Non-Abelian Frame Charge Flow in Photonic Media

Dongyang Wang,[1] Ying Wu,[2] Z. Q. Zhang,[1] and C. T. Chan[1,*]
[1]Department of Physics and Center for Metamaterials Research, Hong Kong University of Science and Technology, Hong Kong, China
[2]Division of Computer, Electrical and Mathematical Science and Engineering, King Abdullah University of Science and Technology (KAUST), Thuwal 23955-6900, Saudi Arabia

(Received 11 September 2022; accepted 7 April 2023; published 16 May 2023)

In *PT*-symmetric systems, the notion of non-Abelian frame charges enables multiband topological characterization of degeneracies by examining the eigenvector-frame rotations. Interestingly, some features of these frame charges can be viewed as an analog of electric charges confined in conducting wires, only that they flow in momentum space along nodal lines. But different from electric charges, these frame charges are not integers, and non-Abelian signatures emerge when braiding between adjacent band nodal lines occurs, which flips the direction of the flow. In photonic systems, the photonic Γ point serves as the source or sink of such a frame charge flow due to a hidden braiding induced by the often-ignored electrostatic mode at zero frequency. This source naturally generates non-Abelian topological signatures in *PT*-symmetric photonic systems that can be identified even in ordinary dielectric media. We use biaxial photonic crystals as examples to show how complex nodal line configurations can be explained as the topological consequences of the frame charge flow from the Γ point to the Brillouin zone boundaries. Our results reveal that non-Abelian band topology is intrinsically manifested in general photonic systems, making them easily accessible platforms for exploring non-Abelian physics.

DOI: 10.1103/PhysRevX.13.021024

Subject Areas: Metamaterials, Optics, Topological Insulators

I. INTRODUCTION

Topological semimetals possess gap-closing degeneracies manifested as nodal points, lines, or surfaces in three-dimensional momentum space [1–21]. These singular nodal features serve as the origin of nontrivial topology and play an important role in topological physics. The topological nature of these nodal degeneracies has been fruitfully characterized using topological invariants such as Chern numbers or quantized Berry phases defined within a single band. Very recently, the topological character of a system where multiple bands are simultaneously considered has been determined and used to characterize the nodal lines in the presence of PT or C_2T symmetry [22,23]. Under such symmetry constraints, the Hamiltonian becomes real. The classifying space of an N-band real Hamiltonian is then $M_N = O(N)/O(1)^N$, where $O(N)$ is the orthogonal group. The first homotopy group of such a Hamiltonian space can be found as $\pi_1(M_N) = Q_N$ [22,24], revealing that generalized quaternions serve as the topological charges. In such an approach, degeneracy lines are topologically characterized by the rotations of the eigenvector frame along 1D loops encircling them. The group Q_N denotes the non-Abelian generalized quaternion or Salingaros vee group of Clifford algebra $\mathcal{C}\ell_{0,N-1}$. It contains 2^N elements, with each generalized quaternion charge q in Q_N formed by the products of generators g_i, which indicate the π rotation of $(i, i+1)$th eigenvectors when the system Hamiltonian goes around the loop.

Within this multiband topology, the real eigenvectors define an orthogonal frame, similar to the axis in Cartesian coordinates, which rotates when the system Hamiltonian evolves in momentum space along a closed loop. The topological charges can then be understood as the quantized angles of the frame rotations around the closed loops, i.e., the frame charges. Distinct from single-band invariants such as Chern numbers, which are integers, quaternions are matrixlike entities that are generally noncommutative under multiplication. The multiband viewpoint thus opens the door to the exploration of non-Abelian topology in energy or frequency bands [22–39]. In addition to providing an understanding of the formation of band degeneracies or the

*Corresponding author.
phchan@ust.hk

prediction of boundary modes, dynamical non-Abelian topological effects may also benefit the pursuit of photonic information processing and quantum logic [40,41]. The path- or sequence-dependent behavior of non-Abelian frame charge evolution also promises potential applications in channel multiplexing or information encryption in optical communication systems.

Despite the recent advances in investigating the nontrivial multiband topology, more intriguing and fundamental features of the non-Abelian frame charges remain to be discovered. As the non-Abelian multiband topology is required to be globally self-consistent, here we take a global perspective that provides access to more fundamental topological characters of the frame charges. Within this context, a momentum-space nodal line characterized by frame charge can be associated with a well-defined sign, so that an "arrow" can be assigned to it [22,25]. Interestingly, the arrow presentation can be heuristically identified as a manner of topological charge flow along nodal lines, which is reminiscent of the classical electric charges flowing in a conducting wire, except that the non-Abelian braidings between nodal lines will induce a sign change or flip of the arrow. Based on the global picture of such a frame charge flow, we first propose a series of novel topological features and then illustrate them with ordinary photonic systems (such as photonic crystals), wherein the equifrequency surfaces intersect each other and manifest as the nodal lines in momentum space. We discuss the governing rule, generating source, and observable topological consequences of the non-Abelian frame charge flow, respectively.

In particular, we find that a hitherto unnoticed role is played by the zero-frequency electrostatic mode in photonic systems. With the zero-frequency mode taken into consideration, the photonic Γ point is a triple degeneracy which makes the photonic eigenstates intrinsically nontrivial from an eigenvector-frame-rotation viewpoint. The zero-frequency band induces a hidden non-Abelian braiding, making the Γ point a source (or sink) of the non-Abelian frame charge flow that has not been discovered before. Such a source character is of fundamental importance in general photonic media that generates the non-Abelian frame charge flow in momentum space. We note that an important role of the zero-frequency mode has also been noticed very recently in determining the minimal band connectivity (when a fundamental complete gap can open) of photonic crystals [42]. We note that the prior work focused on the symmetry indicator of an individual photonic band, where both the method and the scope are very different from this manuscript. Here, we focus on the non-Abelian multiband topological characterization based on eigenvector-frame rotations and homotopy theory that applies to general photonic media, and in fact to any media that have three or more real eigenvectors to define an orthogonal frame.

To be specific, the intersections of equifrequency surfaces in ordinary optical dielectrics of uniaxial or biaxial are shown to manifest the non-Abelian band topology. The topological signatures of a photonic Γ point as a generating source can be identified using conical refraction in the far field. Uniaxial and biaxial photonic crystals are then designed and studied, whose nodal lines evolution (intersection of equifrequency surfaces) in periodic momentum space illustrate the topological frame charge flow, wherein we see that the nodal features can be explained by interpreting the photonic point as a source of frame charges, which flow outward along momentum space nodal lines to Brillouin zone (BZ) boundaries, following an analog of Kirchhoff's law while encountering the BZ boundaries. The emergence of extra nodal lines on the BZ boundaries is enforced as the topological consequences, and their experimental observation substantiates the notion of frame charge flow.

The outline of this paper is as follows. In Sec. II, we propose and illustrate the flowing picture of non-Abelian frame charges with the Kirchhoff-like law and braiding law. In Sec. III, we discuss the non-Abelian band topology embedded in the equifrequency intersections of ordinary photonic media and identify the photonic Γ point as a source of frame charge flow. In Sec. IV, we focus on the topological consequences of such a frame charge flow, including the far-field conical refraction in biaxial dielectric media and the nodal lines evolution in the momentum space of photonic crystals. In Sec. V, we provide direct experimental characterizations of biaxial photonic crystal to verify the topological properties of the nodal lines. Further insights into non-Abelian band topology on a photonic fundamental gap opening are discussed in Sec. VI. Section VII contains a discussion and concluding remarks.

II. NON-ABELIAN FRAME CHARGE FLOW WITH AND WITHOUT BRAIDING

A. General description of frame charge flow

The nodal line is the momentum-space presentation of band degeneracies that are usually protected by symmetries such as a mirror or *PT*. The nodal line carries a quantized Berry phase and can be viewed as a singularity that is the zero limit of a string of Berry curvature [43,44]. In such a way, the nodal line in momentum space plays the role of confinement, where the quantized Berry phase is a result of the enclosed Berry flux by a loop encircling the nodal line. To put this narrative in a heuristic and yet quantifiable description, we can draw an analogy between the topological charges carried by the nodal line and the electrical charges in conducting wire, as shown pictorially in Figs. 1(a) and 1(b). In particular, the magnitude of the "topological charge" in the nodal line can be defined as the quantized Berry phase accumulated along an encircling homotopy loop (π_1), which manifests as the winding of an

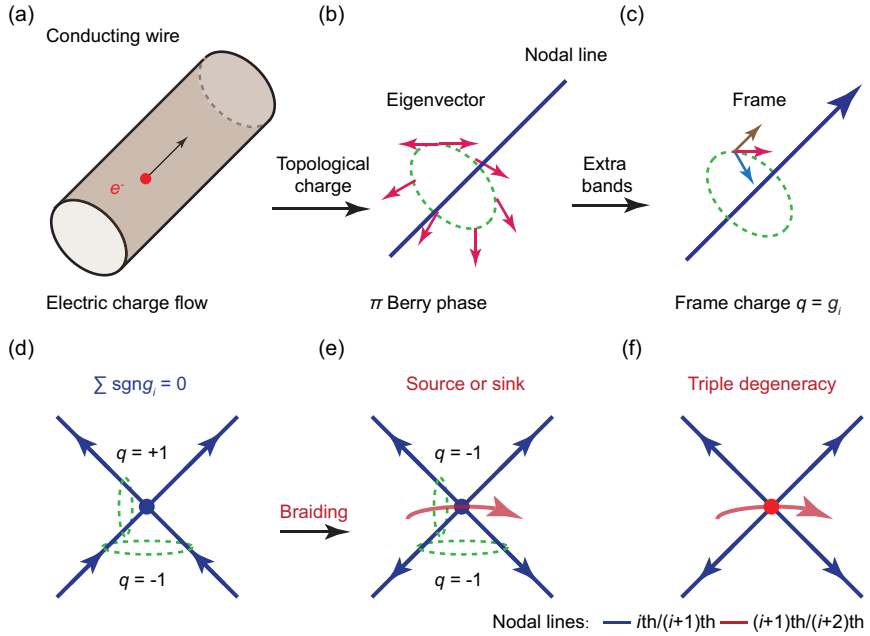

FIG. 1. Non-Abelian frame charge flow with and without braiding. (a) The electric charge moving in a conducting wire in real space. (b) The counterpart of the topological charge (quantized Berry phase) moving along the nodal line in momentum space. (c) The topological charge becomes the non-Abelian frame rotation charge for the PT-symmetric multiband system. (d) When two nodal lines cross each other, the frame charges do not accumulate at the joint point and follow an analog of Kirchhoff's current law. (e) When "braiding" with another nodal line occurs, a sourceless junction point transforms into a source or sink of frame charges with the "all-out" or "all-in" arrows configuration. (f) The braiding can also be manifested as a triple-degeneracy point.

eigenvector. However, in a multiband scenario, the quantized Berry phase becomes a non-Abelian Wilczek-Zee phase [45], and instead of considering the rotation of one single eigenvector, the rotation of the eigenvector frame should be examined, as shown in Fig. 1(c). Depending on whether the frame rotation is "clockwise" or "anticlockwise," a sign can be assigned to the topological frame rotation charge; for instance, the $\pm\pi$ frame rotations are noted as the elements $q = \pm g_i$ of a generalized quaternion group [24] (see Supplemental Material, Sec. I [46]). The sign of frame rotation charge can be presented as the directed arrow on the nodal line, as shown in Fig. 1(c).

When no braiding appears, the charge $q = \pm g_i$ remains conserved for any encircling loop along a nodal line due to the invariance of the topology-determined Wilczek-Zee Berry phase. As such, the frame charges do not accumulate for nodal lines crossing the configuration shown in Fig. 1(d). By incorporating the relative direction regarding the crossing point, it is natural to define the "frame charge flow" following a rule (reminiscent of Kirchhoff's current law) as

$$\sum_n \mathrm{sgn} \times q^n = 0, \tag{1}$$

where n labels and runs over all nodal line branches, and sgn characterizes the flowing direction toward or away from the junction point (in a similar manner to the definition of electric current).

Such a "no-accumulation of charge" can be illustrated by Fig. 1(d), which shows two arrows (or frame charges $q = g_i$) flowing into a meeting point of nodal lines and then flowing out. To characterize the topology with homotopy groups, we encircle the nodal lines with 1D (π_1) loops. Two different ways of encircling a nodal line pair with π_1 loops are illustrated in Fig. 1(d), representing the charge multiplications of $q = \pm g_i$, which result in the $q = +1$ charge (0 frame rotation) and $q = -1$ charge (2π frame rotation), respectively. We note that if the loop encircles two "opposite arrows" (one flowing inward to and the other flowing outward from the junction point), the total charge encircled by the loop is the trivial "+1" quaternion charge, and the encircling of two "same-direction arrows" (either both inward or both outward) gives nontrivial "−1" quaternion charge [22] (see detailed discussion in Supplemental Material, Sec. II [46]).

B. Braiding-induced source or sink

Although these frame charges defined along nodal lines show resemblance to the electric charges flowing in a wire, we note that the frame charge flow can switch sign when braiding occurs due to its non-Abelian character, which happens when one additional degeneracy line comes into action. The non-Abelian nature of frame rotations results in an anticommutative relation between frame charges as $g_{i+1}g_i = -g_i g_{i+1}$, which implies that a braiding between

adjacent nodal lines would introduce a sign change to the frame charge or the arrow direction on a nodal line [22] (explained in Supplemental Material, Sec. II [46]). As the presented case in Fig. 1(e), the existence of another nodal line (the red line) at the junction can flip the arrows on blue nodal lines after they pass through the junction. We thus arrive at the arrow configuration where the arrows are rearranged as all pointing outward from (or inward to) the junction point. Such a braiding point thus functions as a source or sink of the non-Abelian frame charge flow, which has not been reported before. Meanwhile, in such a configuration, any encircled nodal line pairs are with same-direction arrows, and we arrive at the simultaneous topological charges of $q=-1$ for two π_1 loops shown in Fig. 1(e), which fully determine the relative arrow directions around the crossing of two nodal lines. This topological frame charge configuration is referred to as a "double -1" charge in the following for convenience, and it indicates a source or sink of frame charge flow. In Fig. 1(f), we show that such a braiding can also be encoded into a triple-degeneracy point, which corresponds to the photonic band manifestation presented in the next section.

III. NON-ABELIAN BAND TOPOLOGY IN ORDINARY PHOTONIC MEDIA

While the literature might give the impression that abstract notions such as non-Abelian topology are only relevant to very special materials, here we show that they can be manifested in very ordinary optical materials, where the proposed topological features in Sec. II can be found.

In photonic systems, two electromagnetic transverse modes are generally supported due to the polarization degrees of freedom. However, a zero-frequency longitudinal solution is also allowed by Maxwell's equations even though this solution is usually considered to have no consequence in wave propagation. By taking the zero-frequency solution into consideration, the photonic Γ point becomes a threefold degeneracy point, where three eigenvectors define an orthogonal triad frame whose rotation along a k-space loop can be characterized by quaternions and represents the non-Abelian topological charge. In particular, we find that such an intrinsic triple degeneracy at the photonic Γ point serves as the source or sink of non-Abelian frame charge flow in momentum space that we propose in the previous section, where a hidden braiding is embedded at the Γ point making it a generating source.

A. Uniaxial dielectric medium

To reveal the non-Abelian topological features in simple optical media, we start from dielectric materials with only diagonal terms in the permittivity tensor as $\varepsilon=[\varepsilon_{xx},\varepsilon_{yy},\varepsilon_{zz}]$. The Maxwell equations describing such media can be encoded into a three-band Hamiltonian as (details in Appendix A 1)

$$H=\begin{bmatrix} \frac{k_y^2}{\varepsilon_{xx}}+\frac{k_z^2}{\varepsilon_{xx}}+\frac{\omega_{px}^2}{\varepsilon_{xx}} & -\frac{k_xk_y}{\sqrt{\varepsilon_{xx}}\sqrt{\varepsilon_{yy}}} & -\frac{k_xk_z}{\sqrt{\varepsilon_{xx}}\sqrt{\varepsilon_{zz}}} \\ -\frac{k_xk_y}{\sqrt{\varepsilon_{xx}}\sqrt{\varepsilon_{yy}}} & \frac{k_x^2}{\varepsilon_{yy}}+\frac{k_z^2}{\varepsilon_{yy}}+\frac{\omega_{py}^2}{\varepsilon_{yy}} & -\frac{k_yk_z}{\sqrt{\varepsilon_{yy}}\sqrt{\varepsilon_{zz}}} \\ -\frac{k_xk_z}{\sqrt{\varepsilon_{xx}}\sqrt{\varepsilon_{zz}}} & -\frac{k_yk_z}{\sqrt{\varepsilon_{yy}}\sqrt{\varepsilon_{zz}}} & \frac{k_x^2}{\varepsilon_{zz}}+\frac{k_y^2}{\varepsilon_{zz}}+\frac{\omega_{pz}^2}{\varepsilon_{zz}} \end{bmatrix}, \quad (2)$$

whose eigenvalues give the photonic dispersion, and the three eigenvectors represent the polarization states of $[\sqrt{\varepsilon_{xx}}E_x\ \sqrt{\varepsilon_{yy}}E_y\ \sqrt{\varepsilon_{zz}}E_z]$, which together form a rotation frame. The terms involving ω_p are added to allow for the incorporation of resonances.

Taking a dielectric uniaxial material with permittivity $\varepsilon=[2,2,1]$ as an example ($\omega_p=0$), the nodal line in momentum space is shown in Fig. 2(a), where the straight nodal line in blue is formed by the intersection between the equifrequency contours (EFCs) shown in the inset. Taking the zero-frequency solution into account (labeled as the zeroth band), the Γ point is a triple degeneracy that is marked in red. The three-band eigenpolarization frame undergoes a 2π rotation along the π_1 loop encircling the nodal line in momentum space, as shown in Fig. 2(a). The 2π rotation corresponds to the nontrivial -1 element of the quaternion group and remains conserved when the system is adiabatically perturbed (Appendix B 1).

B. Biaxial dielectric medium

More interesting, in a dielectric biaxial material with a permittivity tensor of $\varepsilon=[1,2,3]$, the nodal lines in momentum space become two lines crossing at the photonic Γ point, as shown in Figs. 2(b) and 2(c). In these figures, there exist two loops lying in orthogonal planes (one in the horizontal plane and one in the vertical plane) that both encircle the Γ point and each gives a nontrivial topological charge of -1 manifested as the 2π rotations of the eigenpolarization frame around the loops. The Γ point thus exhibits a double -1 charge, which fully determines the arrow configuration as all pointing outward (or inward). Such an arrow configuration characterizes the photonic Γ point as the source or sink of non-Abelian frame charge flow as we discuss in Sec. II B. Similar to the analysis in Fig. 1(f), the topological origin of the source or sink role here can be traced to the triple degeneracy at the photonic Γ point, which can be intuitively understood as an infinitesimal nodal line formed between the zeroth (zero-frequency mode) and first bands that braids with the blue nodal lines as we present below.

C. Hidden braiding at zero-frequency photonic Γ point

The hidden braiding at the zero-frequency photonic Γ point can be revealed by perturbing the system with the addition of plasmonic resonances, as noted with ω_p in Eq. (2). We take the case of the permittivity tensor as

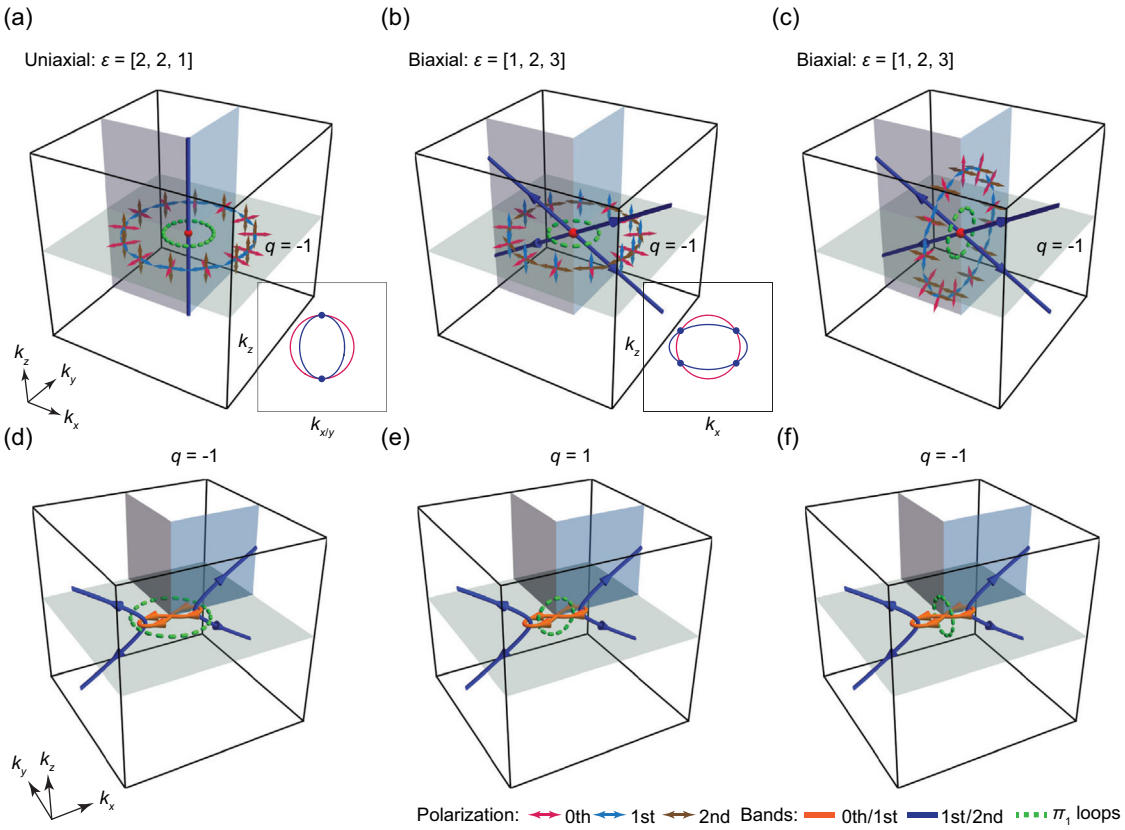

FIG. 2. Frame charge source and hidden braiding in photonic biaxial material. (a) The photonic Γ point is a triple degeneracy by taking the zero-frequency mode into consideration, as marked in red. The nodal line (the intersection of the EFCs from inset) of a uniaxial material gives rise to 2π rotation of the eigenpolarization frame, corresponding to the -1 quaternion charge. (b),(c) Nodal lines of the biaxial material form as the cross structure in momentum space. The two π_1 loops in the horizontal and vertical planes both give 2π frame rotations, which reveals the double -1 charge that generates the frame charge (arrow) flow. (d)–(f) The transformation of nodal lines after introducing the perturbation of $\omega_{px} = 1$ ($\omega_{py,z} = 0$) that reveals the hidden braiding at the photonic Γ point. The original blue nodal line is separated along the k_x direction, but a new orange nodal line shows up to connect them and provides braidings, making the all the arrows on the blue nodal line point outward. The three π_1 loops in (d)–(f) are used to determine the arrows on the nodal lines. The orange nodal line carries a single -1 charge at the Γ point due to the lack of triple degeneracy.

$\varepsilon = [1 - \omega_{px}^2/\omega^2, 2, 3]$ and proceed to study the nodal line transformations and frame charge distribution.

The nodal structures after adding the plasmonic resonance ($\omega_{px} = 1$) are shown in Figs. 2(d)–2(f), where the crossing point of two blue nodal lines is broken, but due to the nontrivial -1 frame charge confinement, the two blue nodal line branches cannot be topologically separated. A new nodal line in orange emerges to link to them, which is formed between one transverse mode and the lifted longitudinal mode (previously zero frequency; see Appendix B 1). Because of the gauge-independent property of the $+1$ and -1 frame charges, we construct a few π_1 loops in Figs. 2(d)–(2f) that encircle two branches of nodal lines of the same color to carry $q = (\pm g_i)(\pm g_i) = \pm 1$ frame charges and study the topological nodal structure.

By calculating the frame charges, the arrows on the nodal lines are determined as indicated in Figs. 2(d)–2(f), and we see that the arrows on the blue nodal lines are all pointing outward similar to the unperturbed case of Figs. 2(b) and 2(c). Importantly, these arrows are induced by the braidings between the orange nodal line and the blue nodal line. As the perturbation tends to zero, the orange nodal line shrinks to infinitesimal and becomes the triply degenerate photonic Γ point. Such a process illustrates the hidden braiding and the origin of double -1 charge at the photonic Γ point of zero frequency.

We note in Figs. 2(e) and 2(f) that the orange nodal line from the zeroth and first bands carries only a single -1 charge at the Γ point (two arrows flow in and another two flow out), which is because the Γ point is no longer a threefold degeneracy after the zero-frequency longitudinal mode is lifted to a finite frequency. Similar results can be found for other types of perturbations (Appendix B 2).

IV. TOPOLOGICAL SIGNATURES INDUCED BY FRAME CHARGE FLOW

A. Far-field identification of the source at the Γ point in a biaxial dielectric

It is known that the conical refraction in biaxial media carries Berry phase information [47,48]. This can be adopted here as a means to identify the topological signatures of arrow configurations on nodal lines around the photonic Γ point. We numerically compute the conical refraction patterns for the four nodal line branches in momentum space of a biaxial material ($\varepsilon = [1, 2, 3]$), as shown in Fig. 3(a). The detailed configuration (modeled in COMSOL MULTIPHYSICS) for observing such conical refractions is shown in Fig. 3(b), where the incident Gaussian beam with circular polarization impinges along the nodal line (or optic axis) direction. While propagating in the biaxial media, a tilted cone shows up, and at the truncated plane, the polarization state experiences a π phase winding, as expected with conical refraction.

To reveal the non-Abelian topology, we examine such phase windings for all four branches of nodal lines as shown in Fig. 3(c), where the observation plane is outwardly pierced by each nodal line branch. The results show that the phase windings are all π on the bright ring of conical refraction. And more importantly, the phase winding directions in the four panels of Fig. 3(c) are all the same (clockwise or anticlockwise depending on the definition), consistent with the all-in or all-out arrow configuration on the nodal lines near the photonic Γ point. These far-field patterns provide evidence for the double -1 charge character of the photonic Γ point, which serves as a source of non-Abelian frame charges in the homogeneous biaxial dielectric.

B. Manifestation of frame charge flow in the periodic Brillouin zone

Since the photonic band of a homogeneous medium extends to infinity in k space in the absence of a minimum length scale, the generated frame charges from the Γ point flow to infinity in momentum space. When seeking additional observable topological signatures induced by the generating source or sink of the photonic Γ point, it is easier to consider periodic photonic crystal systems in which the "flow" of frame charges can be observed within the first Brillouin zone. In the following, we discuss the topological consequences that are identified as momentum-space nodal lines on BZ boundaries and available for experimental near-field measurements.

We design an optically biaxial photonic crystal for experimental demonstration. The unit cell is shown in Fig. 4(a), where two resonators are oriented along orthogonal directions. The metal bars in the resonators have different geometrical lengths of L_1 and L_2. In the long-wavelength limit, the optics of the photonic crystal can be described by the effective permittivity tensor $\varepsilon = [\varepsilon_{xx}, \varepsilon_{yy}, 1]$, where $\varepsilon_{xx} = 1 - \omega_{px}^2/(\omega^2 - \omega_{0x}^2)$ and $\varepsilon_{yy} = 1 - \omega_{py}^2/(\omega^2 - \omega_{0y}^2)$ (Appendix A 2). The frequencies $\omega_{px,y}$ are approximately the same due to the same periodicity of the resonators arranged along the x and y directions. The resonator lengths L_1 and L_2 determine the resonance frequencies $\omega_{0x,y}$ leading to an optically biaxial material with effective permittivity $\varepsilon_{xx} \neq \varepsilon_{yy} \neq 1$ when $L_1 \neq L_2$.

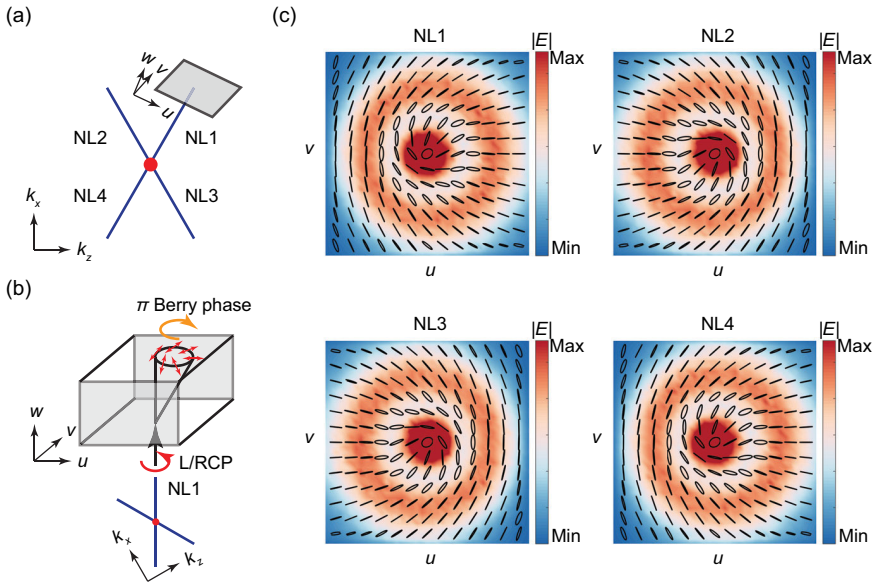

FIG. 3. Conical refractions in biaxial material. (a) The schematic of the examined u-v plane in real space, which is perpendicular to the nodal line branch. (b) The configuration for observing the conical refractions. (c) The winding of polarization states on the conical refraction ring for each nodal line branch.

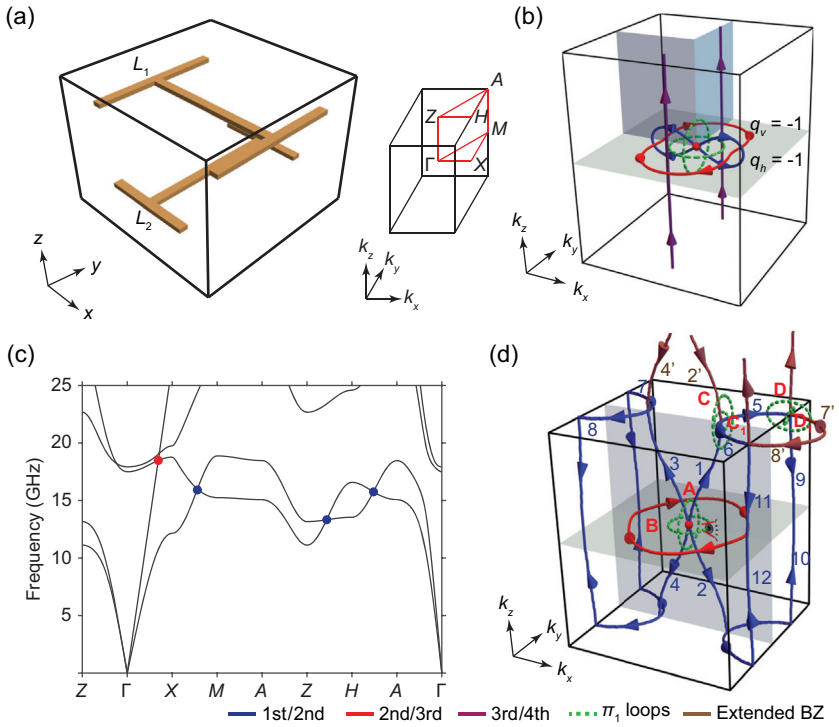

FIG. 4. Non-Abelian frame charge flow in biaxial photonic crystal. (a) Unit cell containing two H-shaped resonators with $L_1 = 3$ mm and $L_2 = 2$ mm. The lattice constants along the x, y, and z directions are $a = 4$ mm, $b = 4$ mm, and $c = 3.2$ mm, respectively. The BZ is shown in the right inset. (b) Nodal structures from the effective Hamiltonian calculation. The Γ point carries a double -1 charge, which can be viewed as the source of non-Abelian frame charge flow, as indicated with directed arrows in color. Adopted parameters are $\omega_{px,y} = 1$, $\omega_{0x} = 0.4$, and $\omega_{0y} = 1.6$. (c) Band structures calculated for the photonic crystal. Degeneracy points are marked in color. (d) Retrieved nodal structure from photonic crystal band dispersions. Brown nodal lines are degeneracies between the first and second bands but join from the extended BZs. Green circles indicate π_1 loops characterizing the -1 (A, B, C, and D) or $+1$ element of the generalized quaternion group (C_1 and D_1). Nodal lines 5–12 can be viewed as topological consequences of the non-Abelian frame charge flow originating from the source at the photonic Γ point.

The low-frequency dispersion of the photonic crystal (near the Γ point) can be described using an effective Hamiltonian (Appendix A 2),

$$\begin{bmatrix} k_y^2+k_z^2+\omega_{px}^2 & -k_xk_y & -k_xk_z & -\omega_{0x}\omega_{px} & 0 \\ -k_xk_y & k_x^2+k_z^2+\omega_{py}^2 & -k_yk_z & 0 & -\omega_{0y}\omega_{py} \\ -k_xk_z & -k_yk_z & k_x^2+k_y^2 & 0 & 0 \\ -\omega_{0x}\omega_{px} & 0 & 0 & \omega_{0x}^2 & 0 \\ 0 & -\omega_{0y}\omega_{py} & 0 & 0 & \omega_{0y}^2 \end{bmatrix} \begin{bmatrix} E_x \\ E_y \\ E_z \\ P_x \\ P_y \end{bmatrix} = \omega^2 \begin{bmatrix} E_x \\ E_y \\ E_z \\ P_x \\ P_y \end{bmatrix}. \tag{3}$$

The eigenvalues are solved to obtain the nodal structures, and the results are shown in Fig. 4(b). Because of the existence of a zero-frequency mode, the eigenvector-frame rotations around the horizontal and vertical π_1 loops (indicated by the green dotted lines) can be both found as 2π (verified in Appendix C 1), indicating that the Γ point is a -1 quaternion charge from the point of view of two orthogonal planes and hence carries a double -1 charge. The nodal lines spawned from the Γ point are each characterized by their own frame charge as indicated by the arrows on them in Fig. 4(b).

Going beyond the effective medium description, we now consider the frame charge flow in periodic momentum space by computing the eigenmodes of the photonic crystal [unit cell shown in Fig. 4(a)] using full-wave simulations (CST Microwave Studio). The band structures are calculated as shown in Fig. 4(c), where high-symmetry positions are marked for the BZ in Fig. 4(a). The band degeneracies are retrieved as momentum-space nodal lines in Fig. 4(d). The Γ point acts as a source (or equivalently, a sink) of non-Abelian frame charge flow. Nodal lines spawning from the Γ point carry frame charges of $q = \pm g_i$ as indicated with

colored arrows on them, with the base point of the homotopy loops pinned near the Γ point.

We then trace the frame charge flow in the periodic BZ of Fig. 4(d) and examine the available topological consequences. Starting from the photonic Γ point, the arrows on the nodal lines labeled as 1–4 all go in outward directions. This is possible due to the double −1 charge at the Γ point, where the −1 charge can be found for both the vertical loop A and horizontal loop B (numerically verified in Appendix C 2). If we follow the frame charge on nodal line 1 from Γ to the top BZ boundary ($k_z = \pi/c$ plane), we notice that the counterpart of nodal line 2 from the extended zone joins it. These lines contribute to a −1 charge ($q = g_1 \times g_1 = -1$) when we consider the π_1 loop C encircling the junction point (verified in Appendix C 2 and discussed in Supplemental Material, Sec. 3 [46] with the Zak phase [34]). This −1 charge fixes the arrow direction on nodal line 2', and the two arrows on nodal lines 1 and 2' are all pointing toward the junction point. To preserve the Kirchhoff-like law, additional nodal lines must emerge from the junction. This explains the existence of two additional nodal lines of 5 and 6 that show up on the top BZ boundary carrying frame charges to point outward from the junction. We then see that the complex network of nodal lines has a topological reason to exist in the way it presents itself, and it is recognized as the topological consequence of frame charge flow. Furthermore, if we follow the nodal lines 5 and 6 to the right BZ boundary, we see that they are joined by nodal lines 7' and 8' from the extended zone. If we consider the π_1 loop D in Fig. 4(d), we find that it encircles a −1 charge, meaning that it must have two arrows of the same sign piercing through the area enclosed by the loop. This requirement enforces the direction of the arrows on nodal lines 5 and 7' to be the same, both flowing toward the junction point. This arrow configuration then requires that additional nodal lines must emerge from the meeting point to satisfy the Kirchhoff-like law, which further explains the emergence of nodal lines 9 and 10' on the right BZ boundary. The Kirchhoff-like law also allows us to assign directional arrows to nodal lines 9 and 10 (or 11 and 12), as shown in Fig. 4(d). We then notice that the arrows on 9 and 10 (or 11 and 12) are flowing in opposite directions, and yet nodal lines 9 and 10 are joined. So, the sign of the quaternion charge on nodal line 9 must be flipped when the charge flow from the top to the bottom of the BZ on the right BZ boundary. This sign-change mechanism is provided by the braiding with the red nodal ring (formed between the second and third bands), remembering that we set the viewpoint (or basepoint) near the Γ point in Fig. 4(d), which makes the red nodal ring lie in front of the nodal lines 9 and 10 to provide braiding. It can also be noticed that the braidings here (between the red nodal ring and nodal lines 9–12) effectively serve as the sink of frame charge flow, complementary to the source at the Γ point. We note again that such a switching is possible because the quaternion group is non-Abelian and there is no Abelian analog, e.g., in electric charges. If we take a look again at the degeneracy points in Fig. 4(c) and the degeneracy lines in Fig. 4(d), it will be difficult to understand why they should appear in such a geometrical arrangement without using the non-Abelian topological interpretation. These nodal line configurations can thus serve as evidence of the frame charge flow, and we provide experimental demonstration in the following.

V. EXPERIMENTAL DEMONSTRATION OF NON-ABELIAN FRAME CHARGE FLOW IN PHOTONIC CRYSTAL

We fabricate the photonic crystal shown schematically in Fig. 4(a) and experimentally characterize the nodal lines on the BZ boundaries to demonstrate the frame charge flow. The samples are fabricated with printed circuit boards (PCBs) and characterized at microwave frequencies. To best present these nodal lines, we focus on the bulk band degeneracies and present the discussions related to surface modes in Supplemental Material, Secs. 3 and 4 [46].

In Figs. 5(a) and 5(b), we show the retrieved nodal lines in the $k_y = 0$ and $k_x = \pi/a$ planes, respectively. These nodal lines can be experimentally characterized with the configuration shown pictorially in Fig. 5(c), where the planar resonators are fabricated on PCBs as arrays of printed metallic elements in the x-y plane. These PCBs are stacked along the z direction to construct a sample exposing the x-z or y-z surfaces.

For the nodal lines in the $k_y = 0$ plane in Fig. 5(a), the nodal degeneracies are the crossing points (marked in green) of the bulk-mode EFCs, as shown in the top row of Fig. 5(d). On the x-z surface of the fabricated sample, we experimentally measure the band projections, and the projected band EFCs are shown in the bottom row of Fig. 5(d). The predicted EFCs can be clearly identified from the measured results as the outer boundaries of excited modes, verifying the nodal lines in the $k_y = 0$ plane.

The nodal lines in Fig. 5(b) can be characterized by cutting the surface BZ (k_y-k_z plane) at discrete k_z positions. In the top row of Fig. 5(e), we show the calculated band projections on the k_y-k_z plane for several k_z-cut lines (scanned along k_y), where the nodal degeneracies can be identified from the projected bands marked with orange dots. In the bottom row of Fig. 5(e), we show the measured results for the projected bands for comparison with the calculation results, and we find very good agreement. The bulk band dispersions with $k_x = \pi/a$ are shown on top of the experimental results as white lines, and the crossing points are identified as orange dots.

In Figs. 6(a) and 6(b), we show the nodal ring in the $k_z = 0$ plane and nodal lines in the $k_z = \pm\pi/c$ plane. These degeneracies can be experimentally identified from the band projections onto the k_x-k_y plane by cutting at different k_x positions (scan along k_y). We show the experimental

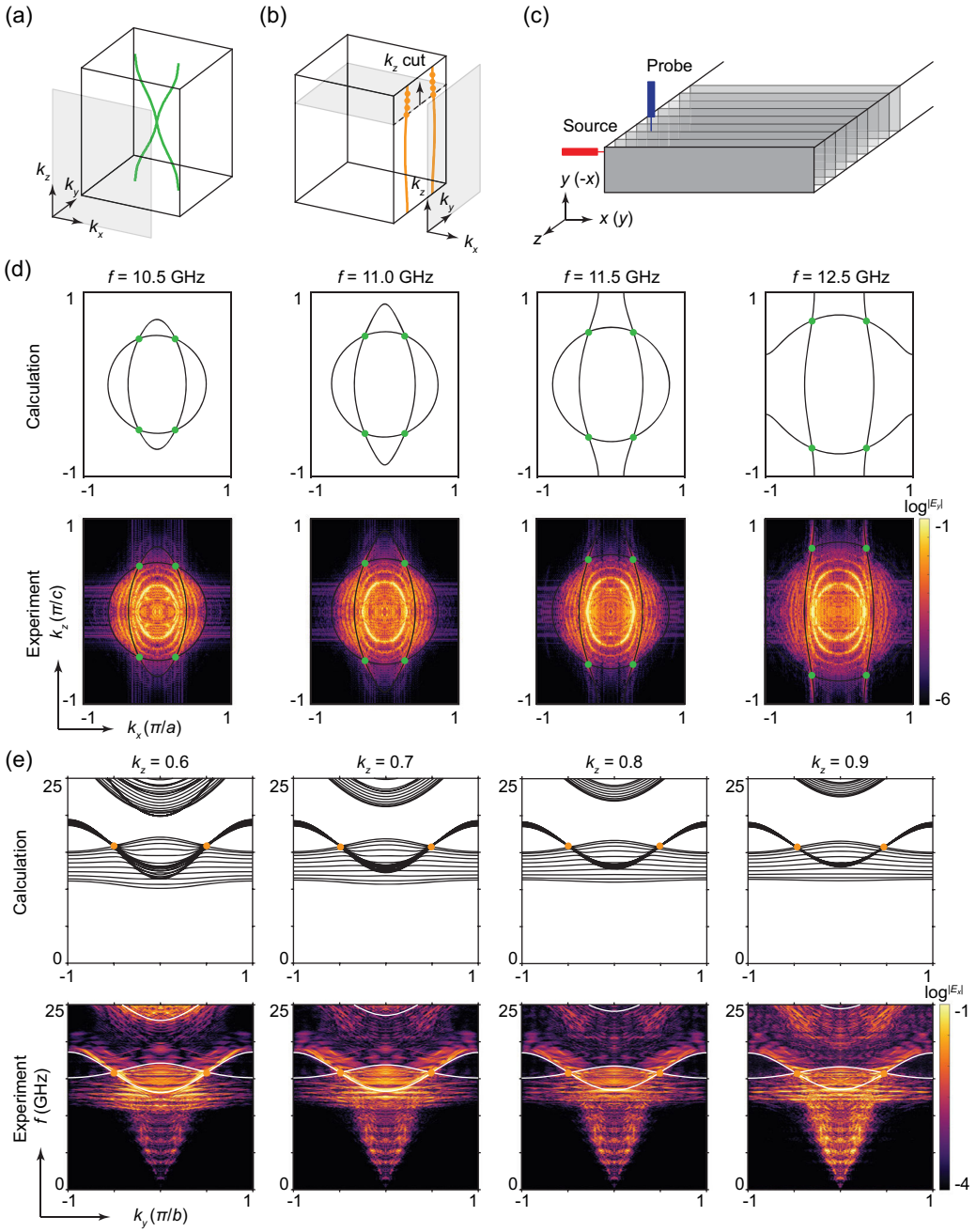

FIG. 5. Experimental characterization of nodal lines on the x-z and y-z surfaces of the biaxial photonic crystal. (a) The nodal line in green is located in the $k_y = 0$ plane and can be measured from the x-z surface. (b) The nodal lines at the $k_x = \pm\pi/a$ boundaries can be characterized from the y-z surface. (c) The experimental configuration for side surface measurements. The PCBs comprising the photonic crystal are stacked horizontally (along the x or y direction, $80 \times 80 \times 10$ units), and the measurements are conducted on the x-z or y-z surface. The source and probe antennas are arranged as indicated. (d) The green nodal line in (a) represents the EFC crossings shown for different frequencies in the top row. Experimentally measured results are shown in the bottom row. (e) Calculated band projection on the k_y-k_z plane with k_z fixed at different values (scan along k_y). Band degeneracies are marked in orange. Experimentally measured results are shown in the bottom row, and bulk bands are plotted as white curves.

configuration in Fig. 6(c), where the PCBs are stacked along the z direction and measurements are conducted at the x-y surface.

At small values of k_x, the nodal ring in the k_x-k_y plane is cut as shown in Fig. 6(a). We show the calculated band projections in the top row of Fig. 6(d). The sliced points from the nodal ring are marked as red dots in the projected bands. Drumhead surface states induced by the nodal ring can be found in the calculated results, which are marked in magenta. Their relationship to the Zak phase is discussed in

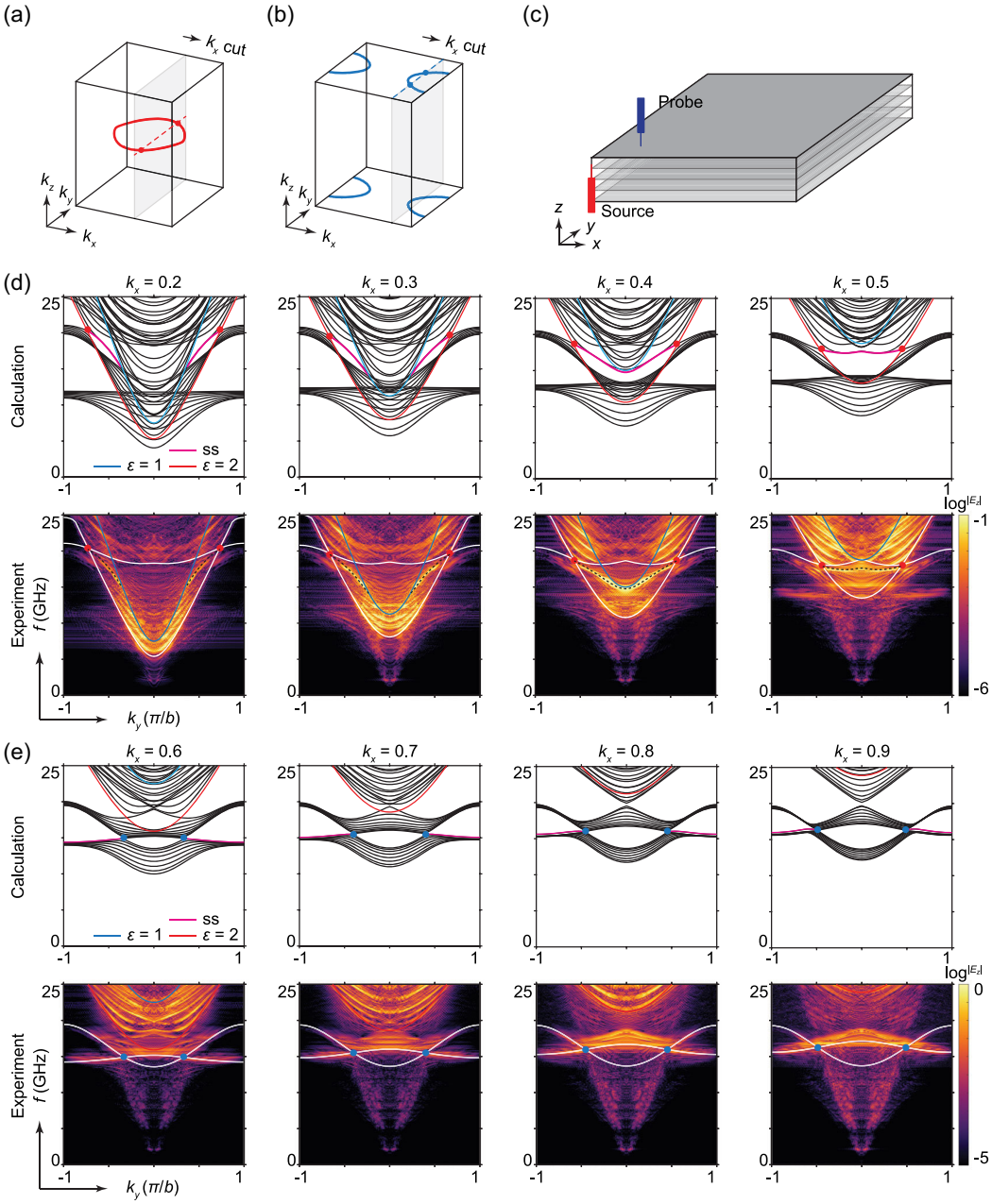

FIG. 6. Experimental characterization of nodal lines on the x-y surface of the biaxial photonic crystal. (a) The $k_x = \text{const}$ plane at small-k_x value cuts the red nodal ring at two nodal points. (b) For large values of k_x, the blue nodal lines are intersected by the $k_x = \text{const}$ plane. (c) Measurement configuration, where PCBs comprising the photonic crystal are stacked along the z direction ($80 \times 80 \times 10$ units). (d) Simulation results for the projected bands at small-k_x values (scanned along k_y) are shown in the first row. Experimentally measured band projections are shown in the second row, with computed band dispersions overlaid as white curves, and the blue line is the light cone. Drumhead surface modes are also experimentally observed. (e) Calculated band projections at large-k_x values are shown in the top row, and the degeneracy nodes are marked in blue. The experimentally measured results are shown in the bottom row, and the computed bulk bands are plotted as white curves.

Supplemental Material, Sec. III [46]. The light cones for the background air ($\varepsilon = 1$) and substrate ($\varepsilon = 2$) are shown as cyan and red curves, respectively. We show the experimental measured results in the bottom row of Fig. 6(d). The bulk bands are shown on top of the experimental results, and the band degeneracy from the nodal ring is identified. The predicted drumhead surface states are also observed in the experimental data, as indicated with black dashed curves in Fig. 6(d).

For larger values of k_x, the nodal lines on the top (or bottom) BZ boundaries are crossed. We show the calculated results in the top row of Fig. 6(e), with the degenerate

positions marked in blue. Light cones for the air and substrate are shown as cyan and red curves, respectively. The experimental measurements are shown in the bottom row, where the predicted degeneracies are observed and marked in blue. We note that the surface modes induced by these nodal lines are closely attached to the bulk bands, as shown in the top row of Fig. 6(e). These surface modes thus merge with the bulk band projections in the experimentally measured results.

We have now experimentally characterized all the nodal lines shown in Fig. 4(d). In particular, the observed nodal lines on the top (bottom) and side BZ boundaries serve as the topological consequence of non-Abelian frame charge flow in momentum space of the biaxial photonic crystal. These nodal lines also provide experimental evidence for the double -1 charge at the photonic Γ point and verify the proposed generating source of frame charge flow.

VI. MULTIBAND TOPOLOGICAL INSIGHT INTO THE OPENING OF THE FUNDAMENTAL PHOTONIC BAND GAP

The opening of the fundamental photonic band gap is one of the most important problems in photonic band-gap systems since the early days of photonic band-gap research [49]. It is constrained by the minimal band connectivity of the lowest set of photonic bands, which has been established recently for the 230 space groups [42,50]. We show here that the multiband topological characterization can offer further insights.

For example, the biaxial photonic crystal shown in Fig. 4 complies with space group no. 47 with a minimal band connectivity of $u = 2$ according to Ref. [42], which permits the gap to be opened between the second and third bands. However, we note that such a gap is not opened in the studied crystal as shown in Fig. 4(c). There are degeneracy rings formed by the second and third bands, and the degeneracy is not "accidental" in the sense that tuning the structural parameters in Fig. 4(a) cannot gap these lines. Interestingly, the existence of the degeneracy can be explained using the flow of frame charge presented in Fig. 4(d). As can be seen in Fig. 4(d), frame charges emerge from the photonic Γ point, and flow along blue nodal lines. They cannot vanish until encountering with a sink, which can be the non-Abelian braidings or unbalanced Zak phases provided at BZ boundaries [34]. With the source configuration of the photonic Γ point (from the zeroth to second bands) shown in Fig. 4(d), direct computation (see Supplemental Material, Sec. III [46]) indicates that there is no additional Zak phase to balance the generating source at Γ, which leaves only one possibility: A sink by braiding is required to exist somewhere inside the BZ. Because of the commutive relation of frame charges for nonadjacent bands [22,25], such a braiding can be provided only by neighbor band-gap closing nodes, which indicates that the second and third bands should be degenerate at some position in momentum space, and that will be the nodal ring in red in Fig. 4(d). The non-Abelian multiband topology thus explains why the minimal band connectivity of $u = 2$ is increased to $u = 3$ for the structure shown in Fig. 4(a). However, we should note that such a multiband topological characterization does not invalidate the minimal band connectivity for the referred space groups, e.g., no. 47 here, found using group theory. There are indeed certain electromagnetic structures of space group no. 47 where the second and third photonic bands are gapped. But there are also structures [e.g., Fig. 4(a)] carrying robust degeneracies between the second and third bands that cannot be gapped by tuning structural parameters (while maintaining the same symmetries), showing that such degeneracies are not accidental. Theses degeneracies can be clearly explained using the non-Abelian multiband topology and the observed higher-band connectivity is topologically protected and hence cannot be broken by changing the system parameters inside the unit cell.

Furthermore, the non-Abelian band topology relies only on PT symmetry, rather than structural symmetry. To illustrate this, we show a uniaxial photonic crystal in Fig. 7, which can be easily achieved by tuning the size of resonator in biaxial photonic crystal as $L_1 = L_2$ in Fig. 4 (thus, $\varepsilon_{xx} = \varepsilon_{yy}$; experimental characterizations are provided in Appendix D). By doing so, the space group transforms from no. 47 to no. 131 ($P4_2/mmc$). As the PT symmetry is still preserved during the geometrical parameter tuning, the non-Abelian frame charge flow along the nodal lines remains robust. It can then be noticed from Fig. 7 that the change of symmetry group affects only the position of nodal lines, not the existence of them, and the requirement of a sink for non-Abelian frame charge also applies here to increase the band connectivity of the presented uniaxial photonic crystal with space group no. 131 (for space group no. 131, the second and third bands can also be gapped according to group theory). Such a geometrical parameter tuning through different symmetry groups exemplifies the robustness of degeneracies in photonic systems that cannot be explained easily using group theory [42,50] but can be straightforwardly understood with non-Abelian multiband topological consideration.

We note that the non-Abelian frame charge characterization provides much more details in the formation and evolution of band degeneracies in momentum space. Take Fig. 4(d) as an example, the non-Abelian band topology provides the reason why nodal lines should spawn from the Γ point and predicts the new nodal lines on BZ boundaries. It also requires the appearance of terminative braidings with adjacent nodal lines. The non-Abelian frame charges also predict the admissible transformations of nodal lines under perturbation, e.g., as shown in Fig. 2. All these features are due to the non-Abelian multiband topology and cannot be obtained directly using group theory.

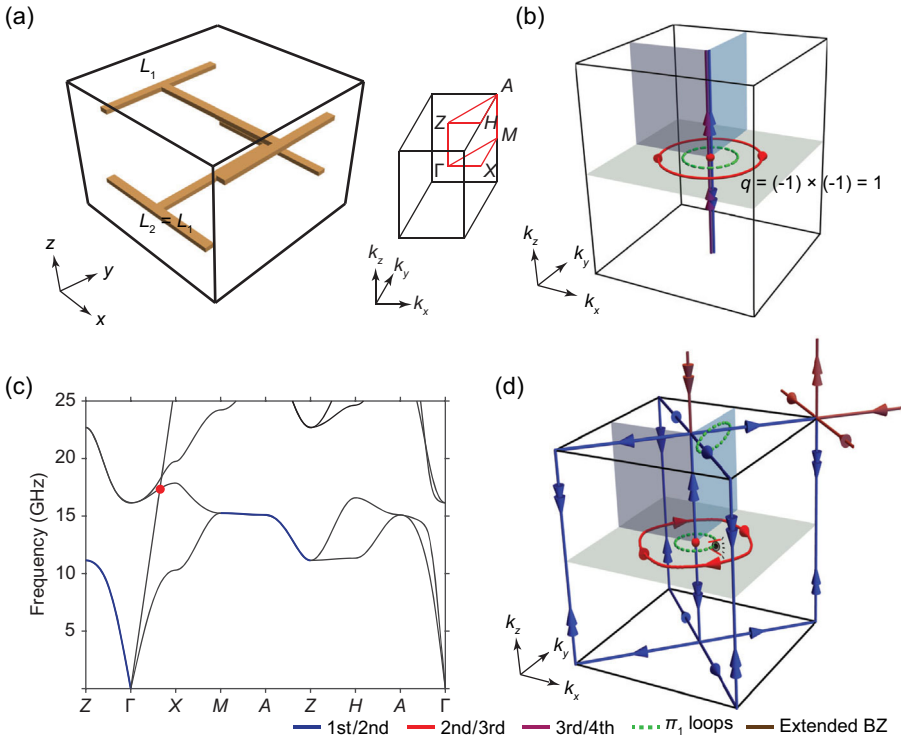

FIG. 7. Non-Abelian frame charge flow in uniaxial photonic crystal. (a) The photonic crystal unit cell with $L_1 = L_2 = 3$ mm. Brillouin zone is shown to the right. (b) Nodal lines calculated from the effective medium model with $\varepsilon_{xx} = \varepsilon_{yy}$ ($\omega_{0x} = \omega_{0y}$), where two straight nodal lines appear along the vertical direction. The overall frame charge for the π_1 loop (green dotted circle) is a result of $q = (-1) \times (-1) = 1$. (c) Calculated band structures for the uniaxial photonic crystal. Degeneracies between the first and second bands can be found along the Γ-Z, M-A, and A-Z degeneracy nodes between the second and third bands are marked red. (d) Nodal structure for the real photonic crystal. The charge-flow-induced nodal lines can still be found at the top, bottom, and side boundaries of the BZ. The green π_1 loops indicate the conserved -1 charge. Base point is shown near the Γ point. Double arrows are adopted to indicate the merging of two linear nodal lines each carrying an arrow.

VII. DISCUSSION AND CONCLUSIONS

The flowing behavior of non-Abelian frame charges is proposed and illustrated in effective media and photonic crystals. The frame charge flow can be both generated and terminated by the non-Abelian braidings and follows a Kirchhoff-like law while flowing along nodal lines. The topological consequences can be found from both far-field observation and momentum-space nodal line evolutions with optical media. The non-Abelian multiband topology also provides further insight into the opening of fundamental photonic band gaps, where we note that the non-Abelian frame charges are required only to be globally self-consistent, and the exact confinement on band connectivity relies on the detail nodal structures in momentum space. In general, the non-Abelian topological confinement on gap opening between the n th and $(n+1)$th bands can be determined by the configuration of nodal lines and Zak phases from the first to n th bands. Therefore, depending on detail conditions, the exact minimal band connectivity of a certain photonic crystal can either remain unchanged or increase to a higher value compared to group theory prediction.

The presented results show that the fundamental multiband non-Abelian topology is embedded in ordinary photonic systems, which generally exists with PT symmetry due to the intrinsic triple degeneracy of the photonic Γ point. By further reducing the PT symmetry to C_2T symmetries, the non-Abelian frame charges are confined to the C_2T-invariant planes, and the Berry flux will emerge and exhibit interestingly similar flowing behavior as the original frame charges. A detailed discussion is provided in Appendix E.

The proposed topological descriptions can also be applied to other multiband systems. For example, phononic systems possess three fundamental bands at the long-wavelength limit, which carry sufficient degrees of freedom to use eigenvector-frame rotation descriptions, and similar topological features can be found (see Supplemental Material, Sec. V [46]).

In conclusion, we propose the flowing behavior of non-Abelian frame charges along nodal lines in momentum space. Some of the behaviors can be viewed as an analog of electric charges flowing along conducting wires in real space, but the possibility of sign flipping (as induced by the passing over of an adjacent nodal line) is uniquely

non-Abelian. Non-Abelian band topology is revealed to manifest itself in general photonic systems, and we show that the photonic Γ point in ordinary optical media is the source or sink of non-Abelian frame charge flow. Such a topological character can be verified through far-field observation. We fabricate a biaxial photonic crystal and experimentally characterize the degeneracy features to demonstrate the frame charge flow in momentum space. Our results shed new light on the fundamental understanding of photonic bands, which could inspire further exploration of the novel non-Abelian physics in ordinary materials and may promote applications in optical communication systems or dynamical physical systems.

ACKNOWLEDGMENTS

We would like to thank Dr. Ruo-Yang Zhang, Dr. Biao Yang, and Professor Shuang Zhang for valuable discussions. This work is supported by Research Grants Council of Hong Kong through Grants No. AoE/P-502/20, No. 16307821, No. 16307621, and No. 16310420 and by the KAUST CRG Grant No. KAUST20SC01.

APPENDIX A: DERIVATION OF THE EFFECTIVE HAMILTONIAN

1. Homogeneous dielectric media

For optical materials with only diagonal terms in permittivity tensor as $\varepsilon=[\varepsilon_{xx}-\omega_{px}^2/\omega^2,\varepsilon_{yy}-\omega_{py}^2/\omega^2,\varepsilon_{zz}-\omega_{pz}^2/\omega^2]$ and permeability of $u=1$, Maxwell's equations can be written as

$$ik_yE_z-ik_zE_y=i\omega\mu_0H_x, \tag{A1a}$$

$$ik_zE_x-ik_xE_z=i\omega\mu_0H_y, \tag{A1b}$$

$$ik_xE_y-ik_yE_x=i\omega\mu_0H_z, \tag{A1c}$$

$$ik_yH_z-ik_zH_y=-i\omega\varepsilon_{xx}\varepsilon_0E_x+V_x, \tag{A1d}$$

$$ik_zH_x-ik_xH_z=-i\omega\varepsilon_{yy}\varepsilon_0E_y+V_y, \tag{A1e}$$

$$ik_xH_y-ik_yH_x=-i\omega\varepsilon_{zz}\varepsilon_0E_z+V_z, \tag{A1f}$$

$$\omega_{px}^2E_x=-i\omega V_x, \tag{A1g}$$

$$\omega_{py}^2E_y=-i\omega V_y, \tag{A1h}$$

$$\omega_{pz}^2E_z=-i\omega V_z, \tag{A1i}$$

where we consider perturbations in the form of plasma resonances, and $\vec{V}=d\vec{P}/dt$ is the time derivative of polarization. Taking $\varepsilon_0=\mu_0=1$, the equations can be encoded into matrices of

$$M=\begin{bmatrix}
0 & 0 & 0 & 0 & k_z & -k_y & -i\omega_{px} & 0 & 0\\
0 & 0 & 0 & -k_z & 0 & k_x & 0 & -i\omega_{py} & 0\\
0 & 0 & 0 & k_y & -k_x & 0 & 0 & 0 & -i\omega_{pz}\\
0 & -k_z & k_y & 0 & 0 & 0 & 0 & 0 & 0\\
k_z & 0 & -k_x & 0 & 0 & 0 & 0 & 0 & 0\\
-k_y & k_x & 0 & 0 & 0 & 0 & 0 & 0 & 0\\
i\omega_{px} & 0 & 0 & 0 & 0 & 0 & 0 & 0 & 0\\
0 & i\omega_{py} & 0 & 0 & 0 & 0 & 0 & 0 & 0\\
0 & 0 & i\omega_{pz} & 0 & 0 & 0 & 0 & 0 & 0
\end{bmatrix}, \tag{A2a}$$

$$N=\begin{bmatrix}
\varepsilon_{xx} & 0 & 0 & 0 & 0 & 0 & 0 & 0 & 0\\
0 & \varepsilon_{yy} & 0 & 0 & 0 & 0 & 0 & 0 & 0\\
0 & 0 & \varepsilon_{zz} & 0 & 0 & 0 & 0 & 0 & 0\\
0 & 0 & 0 & 1 & 0 & 0 & 0 & 0 & 0\\
0 & 0 & 0 & 0 & 1 & 0 & 0 & 0 & 0\\
0 & 0 & 0 & 0 & 0 & 1 & 0 & 0 & 0\\
0 & 0 & 0 & 0 & 0 & 0 & 1 & 0 & 0\\
0 & 0 & 0 & 0 & 0 & 0 & 0 & 1 & 0\\
0 & 0 & 0 & 0 & 0 & 0 & 0 & 0 & 1
\end{bmatrix}, \tag{A2b}$$

and the reformulated Maxwell equations can be written as

$$M\varphi = \omega N\varphi, \tag{A3}$$

with the basis being

$$\varphi = \left[E_x \quad E_y \quad E_z \quad H_x \quad H_y \quad H_z \quad \frac{V_x}{\omega_{px}} \quad \frac{V_y}{\omega_{py}} \quad \frac{V_z}{\omega_{pz}} \right]^T. \tag{A4}$$

The system Hamiltonian can then be derived as

$$H^{9\times 9} = N^{-\frac{1}{2}} M N^{-\frac{1}{2}}. \tag{A5}$$

By taking the matrix square to block diagonalize the Hamiltonian, we can have the simple form of a three-band Hamiltonian:

$$H^{3\times 3} = \begin{bmatrix} \frac{k_y^2}{\varepsilon_{xx}} + \frac{k_z^2}{\varepsilon_{xx}} + \frac{\omega_{px}^2}{\varepsilon_{xx}} & -\frac{k_x k_y}{\sqrt{\varepsilon_{xx}}\sqrt{\varepsilon_{yy}}} & -\frac{k_x k_z}{\sqrt{\varepsilon_{xx}}\sqrt{\varepsilon_{zz}}} \\ -\frac{k_x k_y}{\sqrt{\varepsilon_{xx}}\sqrt{\varepsilon_{yy}}} & \frac{k_x^2}{\varepsilon_{yy}} + \frac{k_z^2}{\varepsilon_{yy}} + \frac{\omega_{py}^2}{\varepsilon_{yy}} & -\frac{k_y k_z}{\sqrt{\varepsilon_{yy}}\sqrt{\varepsilon_{zz}}} \\ -\frac{k_x k_z}{\sqrt{\varepsilon_{xx}}\sqrt{\varepsilon_{zz}}} & -\frac{k_y k_z}{\sqrt{\varepsilon_{yy}}\sqrt{\varepsilon_{zz}}} & \frac{k_x^2}{\varepsilon_{zz}} + \frac{k_z^2}{\varepsilon_{zz}} + \frac{\omega_{pz}^2}{\varepsilon_{zz}} \end{bmatrix}, \tag{A6}$$

and the basis is $\varphi' = [\sqrt{\varepsilon_{xx}}E_x \ \sqrt{\varepsilon_{yy}}E_y \ \sqrt{\varepsilon_{zz}}E_z]^T$.

2. Long-wavelength limit description of photonic crystals

For the metallic photonic crystals shown in Figs. 4 and 7, we describe the EMW's response as

$$\nabla \times \vec{H} = -i\omega\varepsilon_b\varepsilon_0\vec{E} - i\omega\vec{P}, \tag{A7a}$$

$$\nabla \times \vec{E} = i\omega\mu_0\vec{H}. \tag{A7b}$$

Take $\varepsilon_0 = \mu_0 = 1$ and $\varepsilon_b = 1$, and we have

$$\nabla^2\vec{E} = \nabla \times \nabla \times \vec{E} = i\omega\nabla \times \vec{H} = \omega^2\vec{E} + \omega^2\vec{P}, \tag{A8}$$

and consider the Lorentz-type resonance

$$m\frac{d^2\vec{r}}{dt^2} = -m\omega^2\vec{r} = q\vec{E} - m\omega_0^2\vec{r}, \tag{A9}$$

the polarization can be written as

$$\vec{P} = \varepsilon_\infty nq\vec{r} = -\varepsilon_\infty \frac{nq^2}{m(\omega^2 - \omega_0^2)}\vec{E} = -\frac{\omega_p^2}{\omega^2 - \omega_0^2}\vec{E}, \tag{A10}$$

with $\omega_p = \sqrt{\varepsilon_\infty nq^2/\varepsilon_0 m}$, and then we have

$$\vec{D} = \varepsilon_0\vec{E} + \vec{P} = \left(1 - \frac{\omega_p^2}{\omega^2 - \omega_0^2}\right)\vec{E}. \tag{A11}$$

Summarize the above equations together, and we have

$$\nabla \times \nabla \times \vec{E} = \begin{bmatrix} k_y^2E_x + k_z^2E_x - k_xk_yE_y - k_xk_zE_z \\ k_z^2E_y + k_x^2E_y - k_yk_zE_z - k_xk_yE_x \\ k_x^2E_z + k_y^2E_z - k_xk_zE_x - k_yk_zE_y \end{bmatrix}$$
$$= \omega^2\vec{E} + \omega^2\vec{P} = \omega^2\vec{E} + \omega_0^2\vec{P} - \omega_p^2\vec{E}, \tag{A12a}$$

$$(\omega^2 - \omega_{0x}^2)P_x = -\omega_{px}^2E_x, \tag{A12b}$$

$$(\omega^2 - \omega_{0y}^2)P_y = -\omega_{py}^2E_y, \tag{A12c}$$

which can be written into matrix form as

$$\begin{bmatrix} k_y^2 + k_z^2 - \omega^2 + \omega_{px}^2 & -k_xk_y & -k_xk_z & -\omega_{0x}^2 & 0 \\ -k_xk_y & k_x^2 + k_z^2 - \omega^2 + \omega_{py}^2 & -k_yk_z & 0 & -\omega_{0y}^2 \\ -k_xk_z & -k_yk_z & k_x^2 + k_y^2 - \omega^2 & 0 & 0 \\ \omega_{px}^2 & 0 & 0 & \omega^2 - \omega_{0x}^2 & 0 \\ 0 & \omega_{py}^2 & 0 & 0 & \omega^2 - \omega_{0y}^2 \end{bmatrix} \begin{bmatrix} E_x \\ E_y \\ E_z \\ P_x \\ P_y \end{bmatrix} = 0. \tag{A13}$$

Take the substitution of $\vec{P}' = (\omega_0^2/\omega_p^2)\vec{P}$, and we have

$$\begin{bmatrix} k_y^2 + k_z^2 + \omega_{px}^2 & -k_xk_y & -k_xk_z & -\omega_{px}^2 & 0 \\ -k_xk_y & k_x^2 + k_z^2 + \omega_{py}^2 & -k_yk_z & 0 & -\omega_{py}^2 \\ -k_xk_z & -k_yk_z & k_x^2 + k_y^2 & 0 & 0 \\ -\omega_{px}^2 & 0 & 0 & \omega_{px}^2 & 0 \\ 0 & -\omega_{py}^2 & 0 & 0 & \omega_{py}^2 \end{bmatrix} \begin{bmatrix} E_x \\ E_y \\ E_z \\ P_x' \\ P_y' \end{bmatrix} = \omega^2 \begin{bmatrix} 1 & 0 & 0 & 0 & 0 \\ 0 & 1 & 0 & 0 & 0 \\ 0 & 0 & 1 & 0 & 0 \\ 0 & 0 & 0 & \frac{\omega_{px}^2}{\omega_{0x}^2} & 0 \\ 0 & 0 & 0 & 0 & \frac{\omega_{py}^2}{\omega_{0y}^2} \end{bmatrix} \begin{bmatrix} E_x \\ E_y \\ E_z \\ P_x' \\ P_y' \end{bmatrix}. \tag{A14}$$

Then, the Hamiltonian can be formulated as

$$M\varphi = \omega^2 N\varphi, \tag{A15}$$

$$H = N^{-\frac{1}{2}} M N^{-\frac{1}{2}} = \begin{bmatrix} k_y^2 + k_z^2 + \omega_{px}^2 & -k_x k_y & -k_x k_z & -\omega_{0x}\omega_{px} & 0 \\ -k_x k_y & k_x^2 + k_z^2 + \omega_{py}^2 & -k_y k_z & 0 & -\omega_{0y}\omega_{py} \\ -k_x k_z & -k_y k_z & k_x^2 + k_y^2 & 0 & 0 \\ -\omega_{0x}\omega_{px} & 0 & 0 & \omega_{0x}^2 & 0 \\ 0 & -\omega_{0y}\omega_{py} & 0 & 0 & \omega_{0y}^2 \end{bmatrix}, \tag{A16}$$

which satisfies $H\varphi' = \omega^2\varphi'$, with $\varphi' = N^{\frac{1}{2}}\varphi$.

APPENDIX B: DETAILED DESCRIPTION OF DIELECTRIC MEDIA

1. Uniaxial and biaxial dielectrics

For uniaxial and biaxial optical materials, here we provide details about the equifrequency surfaces (EFSs) evolution, nodal structure transformation, manifestation of the -1 charge conservation, and band dispersions.

In Figs. 8(a)–8(c), the EFSs for a uniaxial material with $\varepsilon = [2, 2, 1 - {\omega_{pz}}^2/\omega^2]$ are shown for different frequencies of ω. The EFSs are found as ellipsoids for dielectric uniaxial material in Fig. 8(a), one of which turns into a hyperboloid for $\omega < \omega_{pz}$ when plasmonic resonance is introduced. However, for the frequency of $\omega > \omega_{pz}$, the EFSs turn back into closed surfaces. The corresponding 2D-cut EFCs are shown in Figs. 8(d)–8(f). The degeneracies between the two EFCs contain two transverse modes (first and second bands) with orthogonal polarizations (E_x and E_y) that both propagate along the z direction.

With the perturbation introduced as $\varepsilon = [2, 2, 1 - {\omega_{pz}}^2/\omega^2]$, and $\omega_{pz} = 1$, we see in Fig. 8(g) that the original blue nodal line in Fig. 2(a) breaks into top and bottom branches. However, constrained by the conservation of the -1 charge, which is manifested as the 2π eigenpolarization frame rotation in Fig. 8(g), the two blue nodal lines (formed between the first and second bands) cannot be detached, and an orange nodal line (formed between the zeroth and first bands) emerges to connect the blue nodal lines. To explain in detail, below plasma frequency, the degeneracies between EFCs in Fig. 8(e) collectively form into the orange nodal line, and above the plasma frequency, the degeneracies in Fig. 8(f) form the blue nodal lines. In Fig. 8(h), the manifestation of such degeneracies in band structure is shown, where the flat band at the plasma frequency separates the band structure into two parts, each contributing to the orange and blue colors with different intersection band indices.

Similarly, in Figs. 8(i)–8(k), the EFSs for biaxial material $\varepsilon = [1 - {\omega_{px}}^2/\omega^2, 2, 3]$ are shown for different frequencies. The transition between elliptical and hyperbolic surfaces is similar to the uniaxial case. The 2D-cut EFCs are shown in Figs. 8(l)–8(n). The nodal lines for the biaxial material are shown in Fig. 8(o), where the orange nodal lines can be traced back to the degeneracies in Fig. 8(m), and the blue nodal lines are from the degeneracies in Fig. 8(n). The orange nodal line links to the blue nodal line, since the blue nodal lines cannot separate due to the conservation of -1 frame charge, as verified by the 2π eigenpolarization frame rotation. The band dispersion along the k_x direction is shown in Fig. 8(p), and the longitudinal-mode-induced flat band is shown in orange color.

2. Hidden braidings in biaxial dielectric

We show here the calculated non-Abelian frame charges of the biaxial material when other forms of plasmonic resonance are introduced in additional to the case in Fig. 2. The resonances with ω_{py}, ω_{pz} are introduced in the form of $\varepsilon = [1, 2 - {\omega_{py}}^2/\omega^2, 3 - {\omega_{pz}}^2/\omega^2]$, and the calculated results are shown in Fig. 9. As can be seen in all cases, the perturbations cannot fully separate the blue nodal lines at the Γ point, and new nodal structure always emerges to connect the detached blue nodal line branches. More importantly, the resonance-induced orange nodal line provides braiding with the blue nodal lines, which rearranges the arrow configurations on blue nodal lines as all pointing outward or inward relative to the Γ point. Such results further verify the hidden braiding provided by the triple degeneracy at the Γ point that gives rise to the double -1 charge.

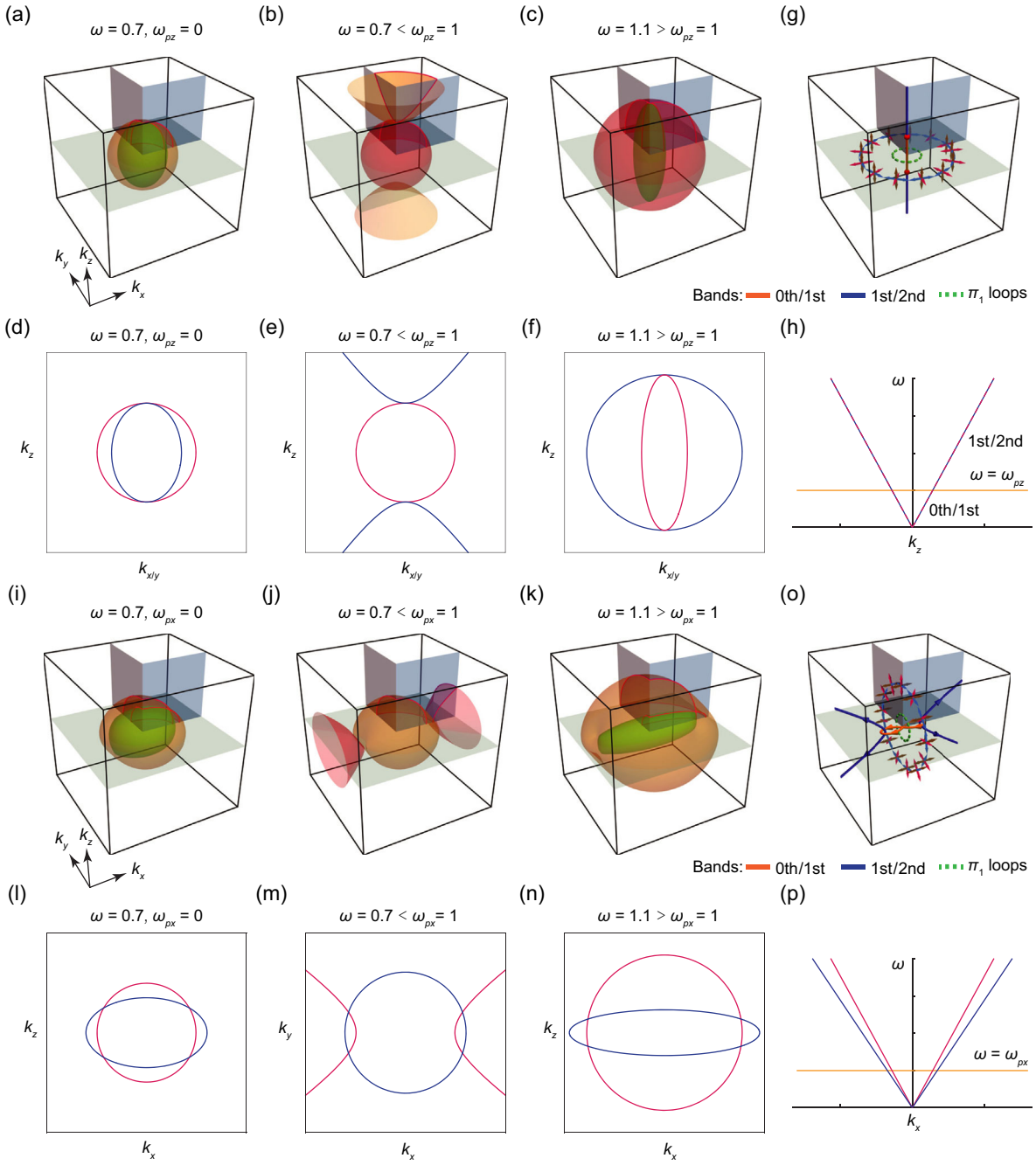

FIG. 8. EFSs and nodal structures for uniaxial and biaxial materials. (a)–(c) The EFSs at different frequencies with $\omega_{pz} = 0$ or 1 ($\omega_{px,y} = 0$). (d)–(f) The EFCs cut from (a)–(c). (g) The nodal line of uniaxial material after introducing perturbation. The orange nodal line (zeroth and first bands) is formed by intersecting EFCs in (e). The blue nodal line (first and second bands) is formed by the degeneracy in (f). (h) The band dispersions for uniaxial material, and the band degeneracy along the k_z direction ($k_x = k_y = 0$) is separated by the flat band at plasma frequency of $\omega_{pz} = 1$ ($\omega_{px,y} = 0$). (i)–(k) The EFSs for biaxial material with $\omega_{px} = 0$ or 1 ($\omega_{py,z} = 0$). (l)–(n) The EFCs cut from (i)–(k). (o) The nodal line in biaxial material with perturbation of $\omega_{px} = 1$ ($\omega_{py,z} = 0$), and the -1 charge and 2π eigenpolarization frame rotation remains unchanged. (p) The band dispersions along the k_x direction for the biaxial material; plasma frequency is at $\omega_{px} = 1$ ($\omega_{py,z} = 0$).

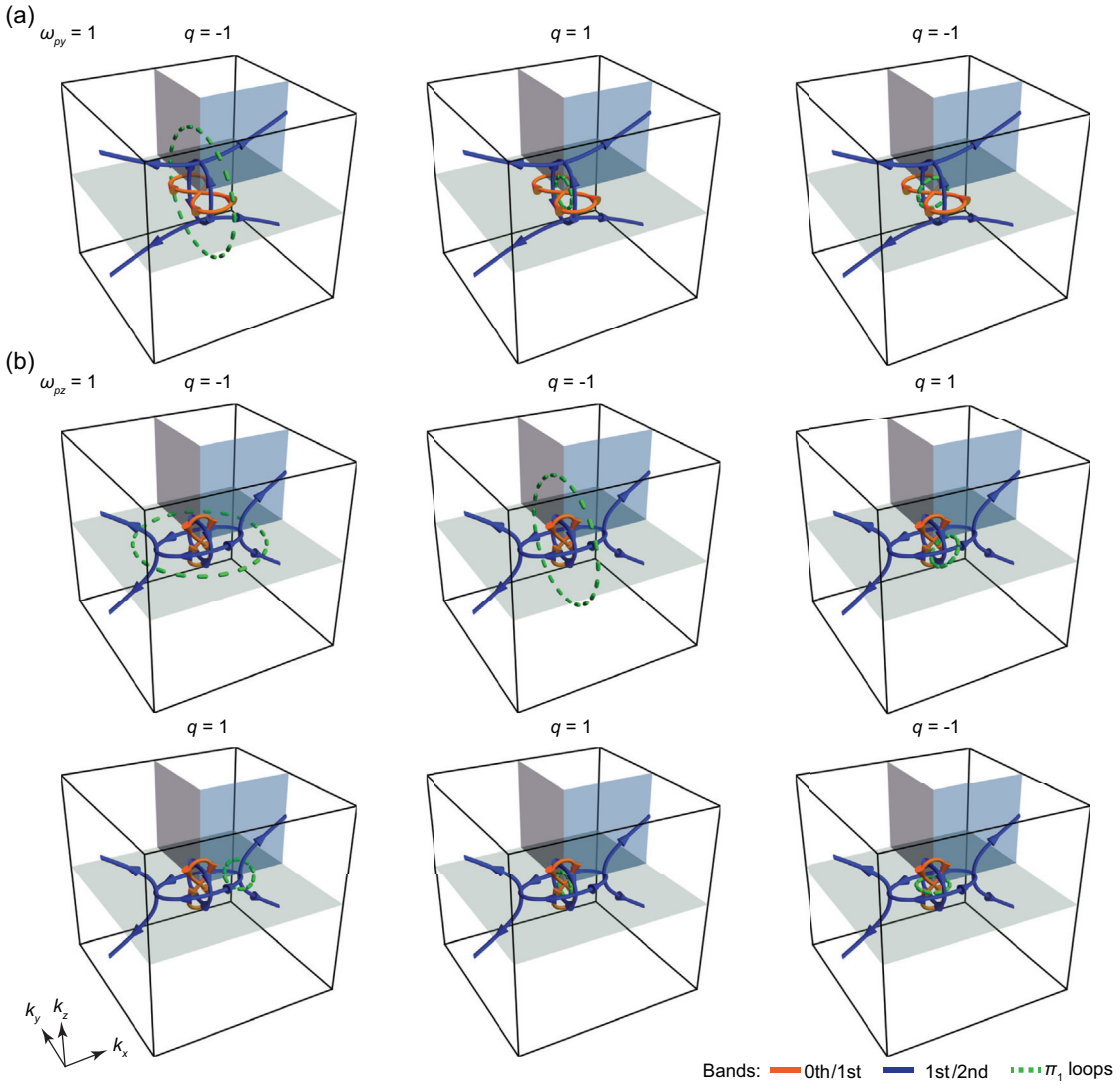

FIG. 9. Hidden braiding in biaxial material. (a) The nodal line transformation after introducing plasmonic resonance of $\omega_{py} = 1$ ($\omega_{px,z} = 0$). The blue chain point is gapped along the k_z direction and connected by the orange nodal line. (b) Similar results for $\omega_{pz} = 1$ ($\omega_{px,y} = 0$); the double -1 charge protection can be verified. The single -1 charge is found for the orange nodal line crossing at the Γ point.

APPENDIX C: FRAME CHARGES IN PHOTONIC CRYSTALS

1. Double −1 charge in biaxial photonic crystal

Based on the effective Hamiltonian formulated for the biaxial photonic crystal in Fig. 4, we check the rotation of polarizations for the two π_1 loops indicated in Fig. 4(b). The results are shown in Figs. 10(a) and 10(b), where the 2π polarization rotations can be found for both π_1 loops. On the three mirror planes in Fig. 10, the $\pm\pi$ rotations can be found for the truncated nodes of the momentum-space nodal lines, where frame charges of $q = \pm g_i$ can be addressed.

2. Eigenvector windings numerically checked for photonic crystal

For the photonic crystal in Fig. 4, we can numerically retrieve the eigenvectors parametrized by wave vector k and verify the non-Abelian frame charge by checking the winding of these eigenvectors. The magnetic part of calculated electromagnetic eigenmodes is taken as $[H_x, H_y, H_z]_k{}^T = \vec{U}_{k,r} e^{ikr}$ and the effective eigenvectors are then formulated as $\overrightarrow{V_k^i} = \sum_r \vec{U}_{k,r}^i$, where i is the band index, and the summarization is over the entire unit cell. The eigenvector windings for the loops indicated in Fig. 4(d) are shown in Fig. 11. We see that the windings

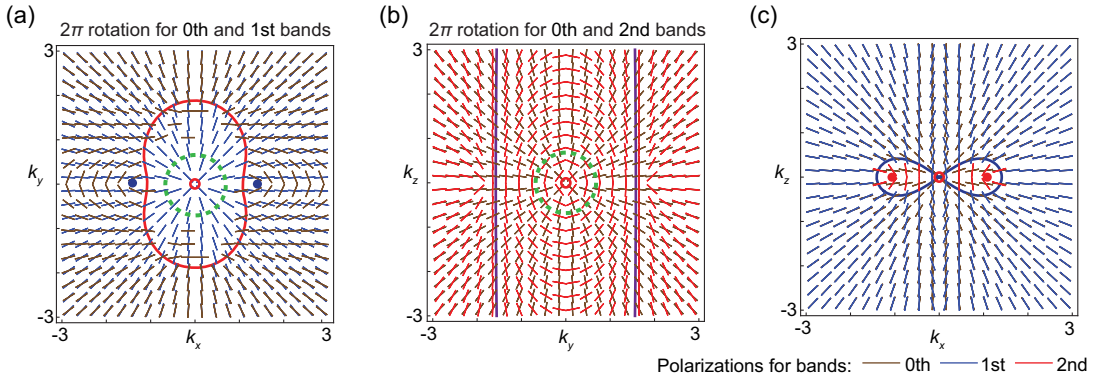

FIG. 10. Double −1 charge verified for the Γ point of the biaxial photonic crystal with effective Hamiltonian. (a) The 2π rotations of polarization for the π_1 loop in the k_x-k_y plane. (b) The 2π rotations of polarization for the π_1 loop in the k_y-k_z plane. (c) The polarization rotations on the k_x-k_z plane. Nodal lines and the truncated nodes on a plane are shown in different colors representing the band indices. Triple degeneracy at the Γ point is marked with hollow dot in red.

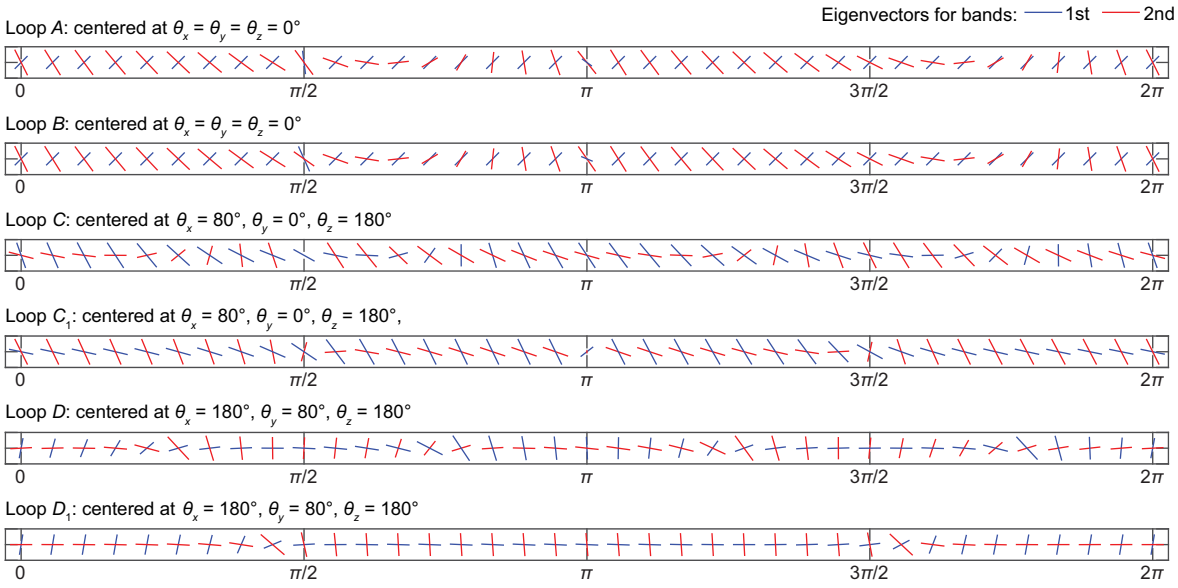

FIG. 11. Eigenvector windings checked for biaxial photonic crystal. The numerically calculated eigenvectors rotate along the π_1 loops in Fig. 4(d). Loops A, B, C, and D carry 2π rotation, and loops C_1 and D_1 present 0 rotation. The values of θ specify the centers of loops, where the first BZ is defined by $\theta = kr \in [-180°, 180°]$ along the k_x, k_y, and k_z directions.

in loops A and B confirm the double −1 charge with 2π rotations. The windings along loops C and C_1 or D and D_1 both verify the Kirchhoff-like law for non-Abelian frame charges, where C and D give 2π windings, and C' and D' give 0 winding.

APPENDIX D: EXPERIMENTAL CHARACTERIZATION OF UNIAXIAL PHOTONIC CRYSTAL

The uniaxial photonic crystal is put to experimental characterization on the y-z surface (PCBs stacked along x). The nodal lines project on the k_y-k_z plane as shown in Figs. 12(a) and 12(b). The nodal lines on the top BZ boundaries project to the surface BZ as straight lines in Fig. 12(a), which can be examined by scanning the band dispersions along k_z at different fixed positions of k_y. On the other hand, the nodal lines on the BZ side boundaries project on the k_y-k_z plane as shown in Fig. 12(b) and can be examined by scanning along k_y at fixed positions of k_z. The experimental configuration for making such measurements is shown in Fig. 12(c) and the field on the y-z surface is measured.

In Fig. 12(d), we first show the calculated results of band projections at fixed-k_y values (scan along k_z), where the band degeneracy points from the nodal line are located at the end points of the projected bands as marked with blue dots. The experimental verifications are shown below the calculation results. Light cones for air and substrate are

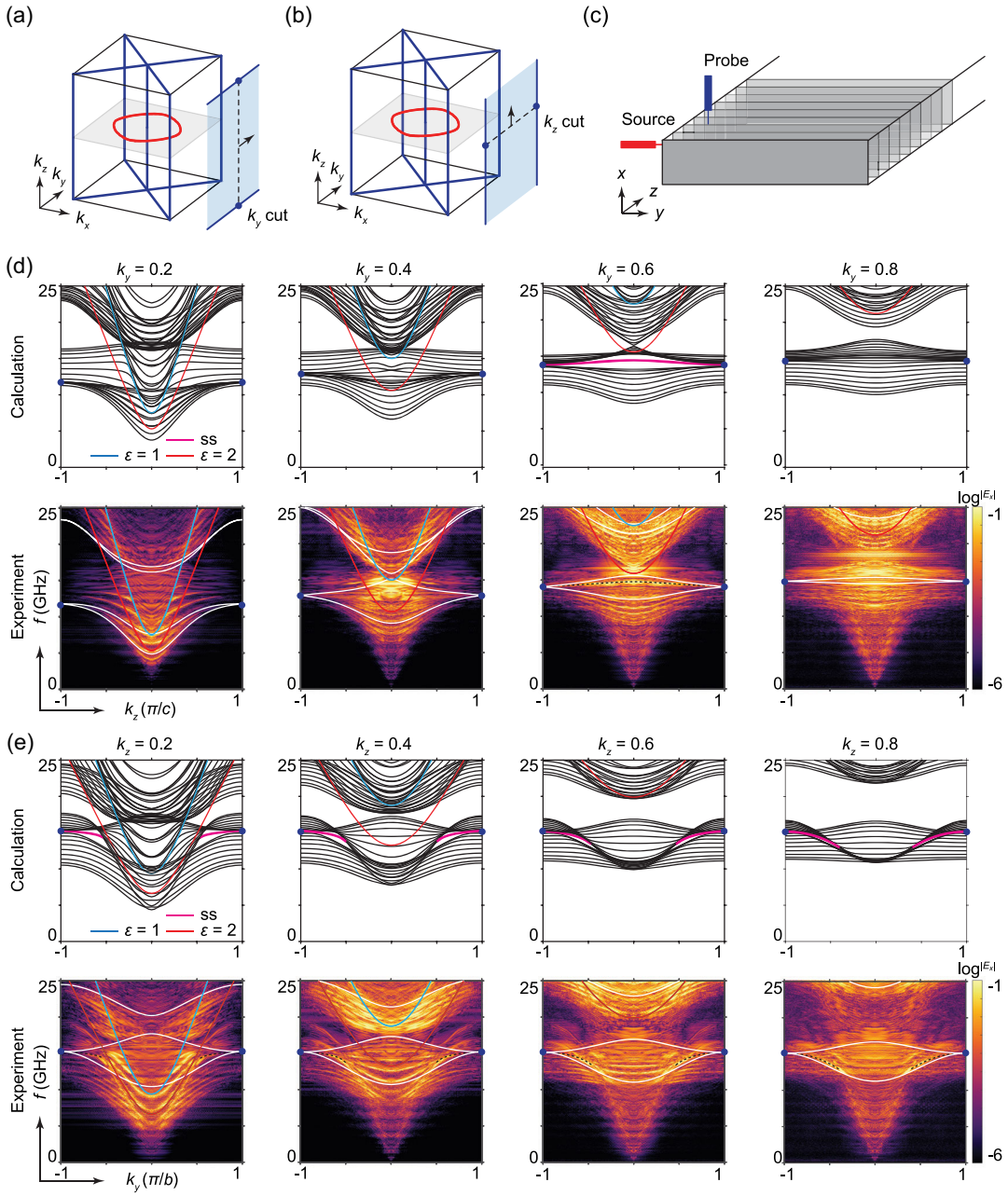

FIG. 12. Experimental characterization of uniaxial photonic crystal. (a) The nodal lines embedded in the top and bottom BZ boundaries project on the k_y-k_z plane. They can be characterized by fixing the k_y value and scanning the band projection along k_z. (b) The nodal lines from the side BZ boundaries can be examined by fixing the k_z values and scanning along k_y. (c) Configuration for the measurement. PCBs are stacked along the z direction. (d) Simulation results and experimentally measured results for the band projections on the k_y-k_z plane at fixed k_y positions (scan along k_z). Surface states are indicated with magenta color and observed in the experiment result at $k_z = 0.6\ \pi/a$ within the projection band gap (indicated with dashed line in black). Light cones for air and substrate are shown with blue and red curves. Bulk band dispersions are plotted on the experimental data in white. (e) The calculated and experimental measured band projections are cut at different k_z values (scan along k_y). Surface states are observed as indicated in the experimental results with dashed black lines.

shown as cyan and red curves. At the position of $k_y = 0.6\ \pi/b$, a gap appears between the projection of the second and third bands, and the surface modes are experimentally observed within the gap, as indicated with dashed line. In Fig. 12(e), the band projection results for fixed-k_z positions are shown (scan along k_y), and both the bulk degeneracies and surface modes are experimentally verified.

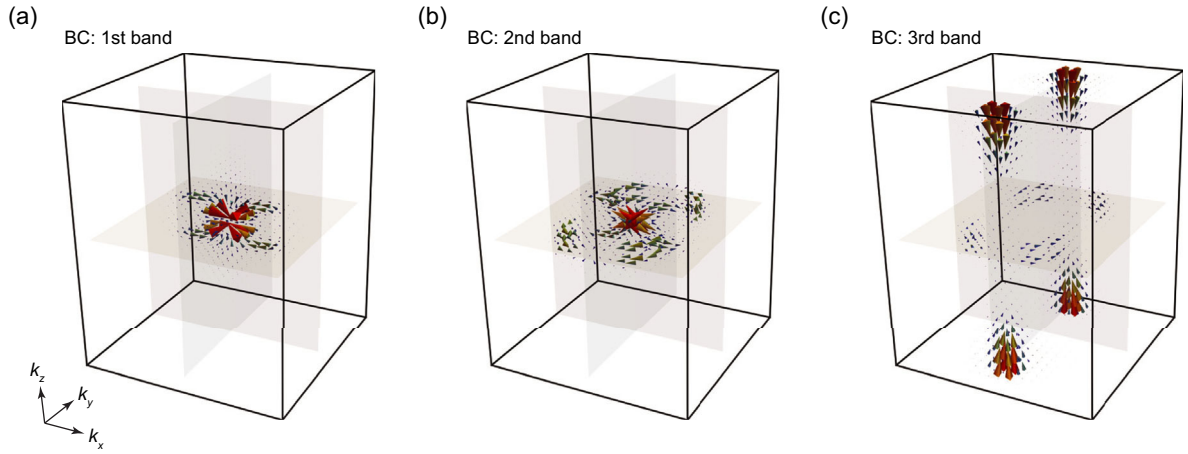

FIG. 13. Berry flux flow under C_2T symmetries. (a)–(c) The Berry curvature calculated for the first to third bands with $\delta = 0.01$. The direction of the Berry flux can be found in accordance with the frame charge flow under PT symmetry.

APPENDIX E: BERRY FLUX FLOW AND FRAME CHARGE FLOW

The nodal line can be acknowledged as the singularities that generate the delta function of the Berry flux directing along the nodal line, which integrates as a quantized Berry phase. It is then natural to seek the correspondence between the non-Abelian frame charge (Wilczek-Zee Berry phase) and the Berry flux emerged by slightly breaking the PT symmetry. We thus introduce perturbations to the effective Hamiltonian of the proposed biaxial photonic crystal in the following form:

$$H = \begin{bmatrix} k_y^2 + k_z^2 + \omega_{px}^2 & -k_x k_y + i\delta k_z & -k_x k_z + i\delta k_y & -\omega_{0x}\omega_{px} & 0 \\ -k_x k_y + i\delta k_z & k_x^2 + k_z^2 + \omega_{py}^2 & -k_y k_z + i\delta k_x & 0 & -\omega_{0y}\omega_{py} \\ -k_x k_z + i\delta k_y & -k_y k_z + i\delta k_x & k_x^2 + k_y^2 & 0 & 0 \\ -\omega_{0x}\omega_{px} & 0 & 0 & \omega_{0x}^2 & 0 \\ 0 & -\omega_{0y}\omega_{py} & 0 & 0 & \omega_{0y}^2 \end{bmatrix}, \tag{E1}$$

where the perturbation is controlled by the parameter of δ. To minimize the influence of PT-symmetry breaking, we break the mirror symmetries but keep the C_2T symmetries on three orthogonal planes. In this way, the non-Abelian frame charges are inherited on the three C_2T- invariant planes.

The symmetry operators of the Hamiltonian can be formulated as $M_x = \mathrm{diag}(-1,1,1,-1,1)$, $M_y = \mathrm{diag}(1,-1,1,1,-1)$, $M_z = \mathrm{diag}(1,1,-1,1,1)$, $C_{2x} = \mathrm{diag}(1,-1,-1,1,-1)$, $C_{2y} = \mathrm{diag}(-1,1,-1,-1,1)$, and $C_{2z} = \mathrm{diag}(-1,-1,1,-1,-1)$, and $T = K$ is the complex conjugate representing time-reversal symmetry. It can then be easily checked that the perturbation with $\delta \neq 0$ breaks all the mirror symmetries, but the three C_2 axes remain along the k_x, k_y, and k_z axes, respectively.

With a weak perturbation strength of $\delta = 0.01$, the Berry curvature is calculated as shown in Fig. 13. The nodal lines break and transform into multiple pairs of Weyl points in momentum space to generate Berry flux. Without detail tracking of the Weyl points distribution, the overall Berry flux behavior shown in Figs. 13(a)–13(c) already presents similarity to the frame charge flow in the PT-symmetric condition. The flowing direction of the Berry flux can be found in accordance with the frame charge flow presented in Fig. 4(b).

[1] L. Lu, J. D. Joannopoulos, and M. Soljačić, *Topological Photonics*, Nat. Photonics **8**, 821 (2014).
[2] T. Ozawa, H. M. Price, A. Amo, N. Goldman, M. Hafezi, L. Lu, M. C. Rechtsman, D. Schuster, J. Simon, O. Zilberberg, and I. Carusotto, *Topological Photonics*, Rev. Mod. Phys. **91**, 015006 (2019).
[3] L. Lu, Z. Wang, D. Ye, L. Ran, L. Fu, J. D. Joannopoulos, and M. Soljačić, *Experimental Observation of Weyl Points*, Science **349**, 622 (2015).
[4] H. Weng, Y. Liang, Q. Xu, R. Yu, Z. Fang, X. Dai, and Y. Kawazoe, *Topological Node-Line Semimetal in*

Three-Dimensional Graphene Networks, Phys. Rev. B **92**, 045108 (2015).

[5] M. Xiao, Q. Lin, and S. Fan, *Hyperbolic Weyl Point in Reciprocal Chiral Metamaterials*, Phys. Rev. Lett. **117**, 057401 (2016).

[6] W.-J. Chen, M. Xiao, and C. T. Chan, *Photonic Crystals Possessing Multiple Weyl Points and the Experimental Observation of Robust Surface States*, Nat. Commun. **7**, 13038 (2016).

[7] D. Wang, B. Yang, W. Gao, H. Jia, Q. Yang, X. Chen, M. Wei, C. Liu, M. Navarro-Cía, J. Han, W. Zhang, and S. Zhang, *Photonic Weyl Points Due to Broken Time-Reversal Symmetry in Magnetized Semiconductor*, Nat. Phys. **15**, 1150 (2019).

[8] C. Fang, Y. Chen, H.-Y. Kee, and L. Fu, *Topological Nodal Line Semimetals with and without Spin-Orbital Coupling*, Phys. Rev. B **92**, 081201(R) (2015).

[9] R. Yu, H. Weng, Z. Fang, X. Dai, and X. Hu, *Topological Node-Line Semimetal and Dirac Semimetal State in Antiperovskite* Cu_3PdN, Phys. Rev. Lett. **115**, 036807 (2015).

[10] T. Bzdusek, Q. Wu, A. Ruegg, M. Sigrist, and A. A. Soluyanov, *Nodal-Chain Metals*, Nature (London) **538**, 75 (2016).

[11] R. Bi, Z. Yan, L. Lu, and Z. Wang, *Nodal-Knot Semimetals*, Phys. Rev. B **96**, 201305(R) (2017).

[12] Z. Yan, R. Bi, H. Shen, L. Lu, S.-C. Zhang, and Z. Wang, *Nodal-Link Semimetals*, Phys. Rev. B **96**, 041103(R) (2017).

[13] P.-Y. Chang and C.-H. Yee, *Weyl-Link Semimetals*, Phys. Rev. B **96**, 081114(R) (2017).

[14] J. Ahn, D. Kim, Y. Kim, and B.-J. Yang, *Band Topology and Linking Structure of Nodal Line Semimetals with* Z_2 *Monopole Charges*, Phys. Rev. Lett. **121**, 106403 (2018).

[15] W. Gao, B. Yang, B. Tremain, H. Liu, Q. Guo, L. Xia, A. P. Hibbins, and S. Zhang, *Experimental Observation of Photonic Nodal Line Degeneracies in Metacrystals*, Nat. Commun. **9**, 950 (2018).

[16] Q. Yan, R. Liu, Z. Yan, B. Liu, H. Chen, Z. Wang, and L. Lu, *Experimental Discovery of Nodal Chains*, Nat. Phys. **14**, 461 (2018).

[17] L. Xia, Q. Guo, B. Yang, J. Han, C.-X. Liu, W. Zhang, and S. Zhang, *Observation of Hourglass Nodal Lines in Photonics*, Phys. Rev. Lett. **122**, 103903 (2019).

[18] D. Wang, B. Yang, R.-Y. Zhang, W.-J. Chen, Z. Q. Zhang, S. Zhang, and C. T. Chan, *Straight Photonic Nodal Lines with Quadrupole Berry Curvature Distribution and Superimaging "Fermi Arcs,"*Phys. Rev. Lett. **129**, 043602 (2022).

[19] H. Park, W. Gao, X. Zhang, and S. S. Oh, *Nodal Lines in Momentum Space: Topological Invariants and Recent Realizations in Photonic and Other Systems*, Nanophotonics **11**, 2779 (2022).

[20] Y. Yang, J.-p. Xia, H.-x. Sun, Y. Ge, D. Jia, S.-q. Yuan, S. A. Yang, Y. Chong, and B. Zhang, *Observation of a Topological Nodal Surface and Its Surface-State Arcs in an Artificial Acoustic Crystal*, Nat. Commun. **10**, 5185 (2019).

[21] M. Xiao, L. Ye, C. Qiu, H. He, Z. Liu, and S. Fan, *Experimental Demonstration of Acoustic Semimetal with Topologically Charged Nodal Surface*, Sci. Adv. **6**, eaav2360 (2020).

[22] Q. Wu, A. A. Soluyanov, and T. Bzdušek, *Non-Abelian Band Topology in Noninteracting Metals*, Science **365**, 1273 (2019).

[23] A. Bouhon, Q. Wu, R.-J. Slager, H. Weng, O. V. Yazyev, and T. Bzdušek, *Non-Abelian Reciprocal Braiding of Weyl Points and Its Manifestation in ZrTe*, Nat. Phys. **16**, 1137 (2020).

[24] P. M. Lenggenhager, X. Liu, S. S. Tsirkin, T. Neupert, and T. Bzdušek, *From Triple-Point Materials to Multiband Nodal Links*, Phys. Rev. B **103**, L121101 (2021).

[25] A. Tiwari and T. Bzdušek, *Non-Abelian Topology of Nodal-Line Rings in PT-Symmetric Systems*, Phys. Rev. B **101**, 195130 (2020).

[26] E. Yang, B. Yang, O. You, H.-C. Chan, P. Mao, Q. Guo, S. Ma, L. Xia, D. Fan, Y. Xiang, and S. Zhang, *Observation of Non-Abelian Nodal Links in Photonics*, Phys. Rev. Lett. **125**, 033901 (2020).

[27] F. N. Ünal, A. Bouhon, and R.-J. Slager, *Topological Euler Class as a Dynamical Observable in Optical Lattices*, Phys. Rev. Lett. **125**, 053601 (2020).

[28] D. Wang, B. Yang, Q. Guo, R.-Y. Zhang, L. Xia, X. Su, W.-J. Chen, J. Han, S. Zhang, and C. T. Chan, *Intrinsic In-Plane Nodal Chain and Generalized Quaternion Charge Protected Nodal Link in Photonics*, Light Sci. Appl. **10**, 83 (2021).

[29] B. Jiang, A. Bouhon, Z.-K. Lin, X. Zhou, B. Hou, F. Li, R.-J. Slager, and J.-H. Jiang, *Experimental Observation of Non-Abelian Topological Acoustic Semimetals and Their Phase Transitions*, Nat. Phys. **17**, 1239 (2021).

[30] Q. Guo, T. Jiang, R.-Y. Zhang, L. Zhang, Z.-Q. Zhang, B. Yang, S. Zhang, and C. T. Chan, *Experimental Observation of Non-Abelian Topological Charges and Edge States*, Nature (London) **594**, 195 (2021).

[31] M. Wang, S. Liu, Q. Ma, R.-Y. Zhang, D. Wang, Q. Guo, B. Yang, M. Ke, Z. Liu, and C. T. Chan, *Experimental Observation of Non-Abelian Earring Nodal Links in Phononic Crystals*, Phys. Rev. Lett. **128**, 246601 (2022).

[32] H. Park, S. Wong, X. Zhang, and S. S. Oh, *Non-Abelian Charged Nodal Links in a Dielectric Photonic Crystal*, ACS Photonics **8**, 2746 (2021).

[33] M. Ezawa, *Non-Hermitian Non-Abelian Topological Insulators with PT Symmetry*, Phys. Rev. Res. **3**, 043006 (2021).

[34] P. M. Lenggenhager, X. Liu, T. Neupert, and T. Bzdušek, *Universal Higher-Order Bulk-Boundary Correspondence of Triple Nodal Points*, Phys. Rev. B **106**, 085129 (2022).

[35] B. Peng, A. Bouhon, R.-J. Slager, and B. Monserrat, *Multigap Topology and Non-Abelian Braiding of Phonons from First Principles*, Phys. Rev. B **105**, 085115 (2022).

[36] B. Peng, A. Bouhon, B. Monserrat, and R.-J. Slager, *Phonons as a Platform for Non-Abelian Braiding and Its Manifestation in Layered Silicates*, Nat. Commun. **13**, 423 (2022).

[37] G. F. Lange, A. Bouhon, B. Monserrat, and R.-J. Slager, *Topological Continuum Charges of Acoustic Phonons in Two Dimensions and the Nambu-Goldstone Theorem*, Phys. Rev. B **105**, 064301 (2022).

[38] S. Park, Y. Hwang, H. C. Choi, and B.-J. Yang, *Topological Acoustic Triple Point*, Nat. Commun. **12**, 6781 (2021).
[39] D. Wang, B. Yang, M. Wang, R.-Y. Zhang, X. Li, Z. Q. Zhang, S. Zhang, and C. T. Chan, *Observation of Non-Abelian Charged Nodes Linking Nonadjacent Gaps*, Phys. Rev. Lett. **129**, 263604 (2022).
[40] O. You, S. Liang, B. Xie, W. Gao, W. Ye, J. Zhu, and S. Zhang, *Observation of Non-Abelian Thouless Pump*, Phys. Rev. Lett. **128**, 244302 (2022).
[41] Y.-K. Sun, X.-L. Zhang, F. Yu, Z.-N. Tian, Q.-D. Chen, and H.-B. Sun, *Non-Abelian Thouless Pumping in Photonic Waveguides*, Nat. Phys. **18**, 1080 (2022).
[42] T. Christensen, H. C. Po, J. D. Joannopoulos, and M. Soljačić, *Location and Topology of the Fundamental Gap in Photonic Crystals*, Phys. Rev. X **12**, 021066 (2022).
[43] K. Kim, J. Seo, E. Lee, K. T. Ko, B. S. Kim, B. G. Jang, J. M. Ok, J. Lee, Y. J. Jo, W. Kang, J. H. Shim, C. Kim, H. W. Yeom, B. Il Min, B.-J. Yang, and J. S. Kim, *Large Anomalous Hall Current Induced by Topological Nodal Lines in a Ferromagnetic van der Waals Semimetal*, Nat. Mater. **17**, 794 (2018).
[44] Y.-M. Xie, X.-J. Gao, X. Y. Xu, C.-P. Zhang, J.-X. Hu, J. Z. Gao, and K. T. Law, *Kramers Nodal Line Metals*, Nat. Commun. **12**, 3064 (2021).
[45] F. Wilczek and A. Zee, *Appearance of Gauge Structure in Simple Dynamical Systems*, Phys. Rev. Lett. **52**, 2111 (1984).
[46] Supplemental Material at http://link.aps.org/supplemental/10.1103/PhysRevX.13.021024 for the introduction to non-Abelian frame charge, characterization of crossing nodal lines with homotopy loops, calculation of Zak phase, and further experimental data.
[47] M. P. Silverman, *The Curious Problem of Spinor Rotation*, Eur. J. Phys. **1**, 116 (1980).
[48] M. V. Berry and M. R. Jeffrey, *Conical Diffraction: Hamilton's Diabolical Point at the Heart of Crystal Optics*, in *Progress in Optics*, edited by E. Wolf (Elsevier, New York, 2007), Chap. 2, pp. 13–50.
[49] K. M. Ho, C. T. Chan, and C. M. Soukoulis, *Existence of a Photonic Gap in Periodic Dielectric Structures*, Phys. Rev. Lett. **65**, 3152 (1990).
[50] H. Watanabe and L. Lu, *Space Group Theory of Photonic Bands*, Phys. Rev. Lett. **121**, 263903 (2018).